UNIVERSITY OF CALIFORNIA, SAN DIEGO

Effects of horizontal advection and vertical mixing on natural iron fertilization in Southern Drake Passage.

A dissertation submitted in partial satisfaction of the requirements for the degree
Doctor of Philosophy

in

Oceanography

by

Marina Frants

Committee in charge:

Sarah T. Gille, Chair
Peter Franks
Greg Mitchell
Keiko Nomura
Dean Roemmich
Lynne Talley

2011

The dissertation of Marina Frants is approved, and it is acceptable in quality and form for publication on microfilm and electronically:

_____

_____

_____

_____

_____

_____
Chair

University of California, San Diego

2011

DEDICATION

This dissertation is dedicated in loving memory to my grandfather, Joseph Rosengaus.

TABLE OF CONTENTS

LIST OF FIGURES

LIST OF TABLES

ACKNOWLEDGEMENTS

I gratefully acknowledge my advisor, Professor Sarah T. Gille, and the members of my committee for their advice and support during the writing of this dissertation. I also extend my thanks to the crews of the *R/V Laurence M. Gould* and the *R/V Nathaniel B. Palmer* and the employees of the Raytheon Polar Services Company, to Dr. Ann Gargett of Old Dominion University, and to Dr. Andrew Thompson of Cambridge University.

VITA

1989	Bachelor of Arts, Fordham University College at Lincoln Center
1991	Master of Science, Massachusetts Institute of Technology
2011	Doctor of Philosophy, University of California, San Diego

FIELDS OF STUDY

Major field: Computer Science
Professor Sirinival Devadas

Major field: Physical Oceanography
Professor Sarah T. Gille

ABSTRACT OF THE DISSERTATION

Effects of horizontal advection and vertical mixing on natural iron fertilization in Southern Drake Passage.

by

Marina Frants

Doctor of Philosophy in Oceanography

University of California, San Diego, 2011

Sarah T. Gille, Chair

A combination of *in situ* and satellite data is used to examine the effects of horizontal advection, diapycnal mixing, and mixed-layer entrainment on natural iron fertilization in a region near the Shackleton Fracture Zone in southern Drake Passage. Results from Optimal Multiparameter analysis of temperature, salinity, oxygen and nutrient data are consistent with a scenario in which iron-rich shelf waters from the South Shetland Islands and the Antarctic peninsula are advected northward on the eastern side of the Shackleton Transverse Ridge (STR), where they interact with the low-iron waters of the Antarctic Circumpolar Current (ACC) in the Ona Basin. However, comparisons between sea surface height and Chlorophyll-a (Chl-a) levels in the region for the years 1997-2010 indicate that this advection process is significantly correlated with biological productivity only during the months of November and December, while high Chl-a concentrations persist through March. Enhanced diapycnal mixing and mixed-layer entrainment are considered as alternative mechanisms for delivering iron into the Ona

Basin mixed layer. While fine-scale mixing estimates lack the vertical resolution to fully resolve the small-scale density fluctuations in the low-stratification regime of the Southern Ocean, microstructure measurements indicate that diapycnal diffusivities in Drake Passage are on the order of 10^{-4} m^2 s^{-1}. Based on these diffusivities, estimates of iron flux from iron concentrations measured during the summer of 2004 and winter of 2006 suggest that diapycnal mixing alone can supply iron ito the mixed layer at a rate of approximately 96$\pm$9 nmol m^{-2} day^{-1} during the winter and approximately 64$\pm$2 nmol m^{-2} day^{-1} during the summer. In addition, the Ona Basin mixed layer deepens from January into April, allowing for iron to be steadily entrained from below. Simulation of these vertical processes with a simple one-dimensional model yields an estimated mixed-layer entrainment rate of 12$\pm$9 nmol m^{-2} day^{-1}, while the combined effect of mixing and entrainment can supply 176$\pm$44 nmol m^{-2} day^{-1} into the top 30 m from January to April, which is sufficient to sustain the phytoplankton bloom that persists in the basin throughout the summer months.

Chapter 1

Introduction

The Southern Ocean is the world's largest high-nitrate, low-chlorophyll (HNLC) oceanic region in the world, meaning that its phytoplankton biomass, as estimated from levels of phytoplankton chlorophyll, are low relative to the amount of inorganic nutrients present in the water. Satellite-based and *in situ* measurements of phytoplankton abundance show a highly heterogeneous distribution, with regions of high phytoplankton biomass occurring primarily in shallow waters near islands and continental margins and in deeper waters located downwind and downstream from land features that interrupt the flow field of the Antarctic Circumpolar Current (ACC) between 45° and 60°S (Blain et al., 2001; Sullivan et al., 1993). Since biological productivity in the pelagic Southern Ocean is primarily iron-limited (Martin et al., 1990; Chisholm and Morel, 1991; de Baar et al., 1995; Boyd, 2002), these observations suggest that phytoplankton biomass in the open ocean is increased by the redistribution of iron from shelf waters into pelagic waters in regions where mixing between waters from different sources is enhanced by topographic features (Holm-Hansen et al., 2005). However, the physical processes that drive the regional differences in iron distribution are not yet well understood (de Baar and de Jong, 2001). A number of possible mechanisms have been examined. Whitehouse et al. (2008) found evidence of nutrient upwelling resulting from diverging flow of the ACC over the shelf near South Georgia Island. Sokolov and Rintoul (2007b)

have found that similar upwelling occurs wherever the ACC interacts with topography. Hewes et al. (2009) observed that shallow mixed-layer depths contribute to increased Chl-a levels near the South Shetland Islands. *In situ* observations near the Kerguelen Plateau (Blain et al., 2001) and the Crozet Plateau (Venables et al., 2007) suggest that sediment mixing in shallow waters near islands and continental shelves, followed by downstream advection, can supply iron to facilitate blooms in off-shore waters.

Biological productivity in the Southern Ocean plays a disproportionately significant role in the functioning of the global carbon cycle. Paleoceanographic evidence indicates that during periods of increased iron supply and enhanced production, the biological pump functions more efficiently, increasing the rate of absorption of carbon dioxide from the atmosphere into the ocean (Broecker and Henderson, 1998). Since atmospheric CO_2 is a major contributing factor to global warming, understanding the mechanisms of iron supply in the Southern Ocean can lead to a better understanding of the processes that govern global climate change.

The goal of this dissertation is to examine the physical mechanisms that affect natural iron fertilization in the Shackleton Fracture Zone (SFZ), a region located in the vicinity of the Shackleton Transverse Ridge (STR) in southern Drake Passage. The circulation in this region is marked by high eddy activity and a high degree of temporal variability as the ACC is steered by the bathymetry. Satellite-derived images of Chlorophyll-a (Chl-a) distribution show a persistent and well-defined front, with low Chl-a waters located to the west of the STR, and high Chl-a in the Ona Basin to the east. The region of high Chl-a coincides with the region where the Southern ACC Front (SACCF) moves off-shore, potentially allowing the iron-rich shelf waters near the Shetland Islands and the Antarctic peninsula to propagate into the Ona Basin and interact with the low-iron waters of the ACC. In addition, flow of the ACC over the variable bathymetry of the SFZ leads to enhanced diapycnal mixing, exceeding background open ocean levels by an order of magnitude. Mixed-layer depth in the region also varies, deepening steadily during the summer months and allowing for entrainment of additional iron from the top of the pycnocline. All of these processes – horizontal ad-

vection, mixing, and entrainment – can potentially influence the iron levels in the mixed layer in the Ona Basin.

Chapter 2 of this dissertation uses Optimal Multiparameter analysis (Tomczak and Large, 1989) to describe the horizontal circulation in the SFZ, focusing on the relative contributions of shelf waters and ACC waters to the water composition in the Ona Basin over the density range where iron levels are highest. The data set used for the study consists primarily of shipboard CTD and expendable CTD (XCTD) measurements of temperature and salinity, sampled in the SFZ during the summer of 2004 and winter of 2006. Iron and nutrient data from both cruises are included in the analysis.

Chapter 3 examines the accuracy of two commonly used methods of estimating kinetic energy dissipation rate ϵ and diapycnal eddy diffusivity κ from fine-scale data. Values for κ for Drake Passage and for the eastern Pacific sector of the Southern Ocean are estimated from CTD and XCTD data collected during the Diapycnal and Isopycnal Mixing Experiment in the Southern Ocean (DIMES) in summer 2010. The Thorpe scale method (Thorpe, 1977) and the vertical strain method (Gregg and Kunze, 1991) are used to compute the estimates. High-resolution profiles of temperature and salinity were sampled concurrently with the CTD and XCTD profiles, providing a unique opportunity to calibrate the fine-scale mixing estimates against the more precise microstructure measurements. Based on the instrument noise and spectral properties of the CTD and XCTD measurements, as well as comparisons between fine-scale and microstructure estimates, we conclude that in the low-stratification regime of the Southern Ocean, fine-scale estimates cannot reliably distiguish small-scale turbulence from instrument noise.

Chapter 4 builds on the previous two chapters to examine the relative contributions of horizontal and vertical processes on the mixed-layer iron concentrations in the SFZ. First, satellite-derived sea-surface height (SSH) and Chl-a data, discussed in Section 4.2, are used to examine the correlation between the monthly Chl-a concentrations in the Ona Basin and the horizontal advection of shelf-waters caused by the off-shore meandering of the SACCF. Then, typical Drake Passage values of κ, as discussed in Chapter 3, are applied to iron profiles from the Ona Basin to estimate the daily flux of

iron into the base of the mixed layer due to diapycnal mixing. Mixed-layer estimates from two Southern Ocean climatologies (de Boyer Montegut et al., 2004; Dong et al., 2008), as well as from *in situ* data, are used to make a preliminary estimate of the daily entrainment rate of iron from the top of the pycnocline. Finally, a one-dimensional mixed-layer model (Price et al., 1986) is used to calculate the combined effect of mixing and entrainment on the daily mixed-layer iron concentrations during the summer months.

Chapter 2

Optimal Multiparameter analysis of source water distributions in southern Drake Passage

2.1 Introduction

In this chapter, we examine the water properties in the Shackleton Fracture Zone (SFZ) in Southern Drake Passage near the Antarctic Peninsula (Figure 2.1a). The Shackleton Transverse Ridge (STR) runs diagonally across the SFZ, extending northwest into Drake Passage from Elephant Island (see Figure 2.1b). The shallowest depth over the ridge is approximately 800 m, while the basins on either side reach depths of over 4000 m; the gap between the ridge and Elephant Island has a depth of over 3000 m. The flow of the ACC around the topography creates a region of high mixing, as the meridional meandering of the Southern ACC Front (SACCF) brings the ACC waters into close proximity with the shelf waters off the Antarctic Peninsula and the South Shetland Islands (Orsi et al., 1995), as well as with the Weddell Sea waters flowing north toward the Scotia Sea (Barré et al., 2008; Brandon et al., 2004; von Gyldenfeldt et al., 2002; Whitworth et al., 1994).

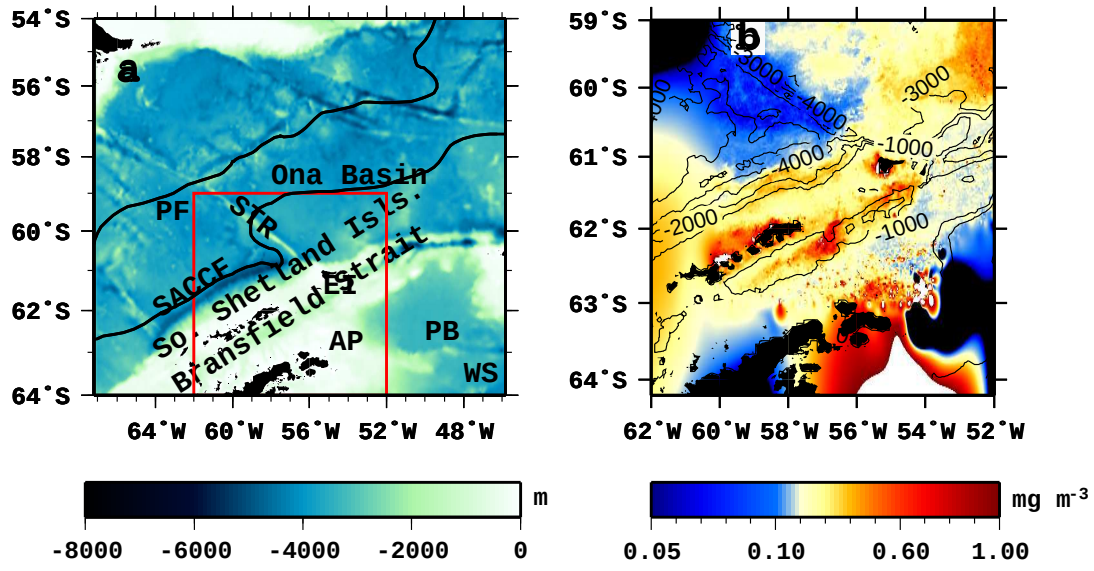

Figure 2.1: (a) Drake Passage bathymetry with study region indicated by the red rectangle. Front definitions are taken from Orsi et al. (1995). The abbreviations are: Shackleton Transverse Ridge (STR), Elephant Island (EI), Polar Front (PF), Southern ACC Front (SACCF), Antarctic Peninsula (AP), Powell Basin (PB) and Weddell Sea (WS). (b) A composite of Chl-a distribution in the study region from January 1 to March 31 2004, computed from SeaWiFS and MODIS-Aqua satellite data.

Satellite-derived Chlorophyll-a (Chl-a) images in this region (Kahru et al., 2007) show a sharp gradient in surface chlorophyll levels in the vicinity of the STR (Figure 2.1b). Low Chl-a water is located to the west of the ridge, and high Chl-a water is found to the east in the Ona Basin and continues downstream into the southern Scotia Sea. Shipboard iron incubations conducted across the gradient have shown that phytoplankton biomass in the western Drake Passage is iron-limited, except in the shallow waters on the continental shelf (Helbling et al., 1991; Hopkinson et al., 2007). The incubation results, together with the low iron levels measured in the ACC west of the STR by Martin et al. (1990), the iron distributions reported by Ardelan et al. (2010), and the Chl-a distributions shown by Kahru et al. (2007), suggest that the Ona Basin consistently has higher levels of iron than the surrounding waters.

Previous studies of hydrographic data in the vicinity of the SFZ and the Antarctic Peninsula show the presence of Circumpolar Deep Water (CDW), Bransfield Strait Water (BW) and Weddell Sea Deep Water (WSDW) (Zhou et al., 2010b; Hofmann et al., 1996; Whitworth et al., 1994). The water column of the ACC is characterized primarily by CDW, overlaid by Antarctic Surface Water (ASW) during the summer. On the continental shelf, interaction between these water masses, combined with the effects of local cooling, ice melt and precipitation effects, form the shelf waters (Hofmann et al., 1996; Zhou et al., 2002, 2010b). Shelf waters flow northward from the Weddell Sea and branch at the northern tip of the peninsula, with some of the waters flowing eastward into the Weddell-Scotia Confluence and some flowing westward and contributing to the formation of the BW (Hofmann et al., 1996; Zhou et al., 2002). The BW, in turn, combines with the CDW from the ACC to form the shelf waters around the South Shetland Islands (Hofmann et al., 1996; Zhou et al., 2002). Since the shelf waters are iron-rich compared to the ACC waters (Hopkinson et al., 2007), their distribution affects biological productivity throughout the SFZ.

Optimal Multiparameter Analysis (OMP) (Tomczak and Large, 1989) allows us to estimate the relative contributions of these waters for a region comprising the deep basins to the east and west of the STR, the gap to the south of the STR, and the conti-

nental shelf along the South Shetland Islands. Our analysis is based on the assumption that advection moves water primarily along isopycnals; therefore we examine source water distributions for the isopycnal layer where the iron concentrations are highest in both summer and winter. We also perform the analysis for the density range below the iron peak, in order to evaluate whether the upper-ocean flow in the region shows the same high degree of vertical coherence as observed by previous ADCP measurements in southern Drake Passage (e.g. Lenn et al., (2007)). A vertically coherent flow would help preserve the iron peak and gradients as the iron advects off the shelf and into the basin. This approach allows us to assess quantitatively the horizontal propagation of iron-rich shelf waters within our study region.

Section 2.2 describes the data and sampling methods used for our study. Section 2.4 provides a detailed discussion of our choice of density range for the OMP analysis, based on the iron distribution in the study area and the location of the iron peak. The selection of the stations that define the source water properties for the analysis is described in Section 2.5, and the results of the OMP analysis are discussed in section 2.6.

2.2 Data

2.2.1 Cruise data

Two cruises were conducted in the vicinity of the STR to study oceanographic transport and its possible influence on biological activity in the Ona Basin. In February and March 2004, the *R/V Laurence M. Gould* (LMG0402) collected hydrographic, chemical and biological data in the vicinity of the STR. In July and August 2006, the *R/V Nathaniel B. Palmer* (NBP0606) revisited the area to collect similar measurements. In addition, a survey by the U.S. Antarctic Marine Living Resources (AMLR) Program was conducted in January and February of 2004, overlapping with LMG0402. The locations of all the hydrographic stations are shown in Figure 2.2.

A total of 121 casts were made during LMG0402, and 192 casts were made

during NBP0606, all to 1000 m or 10 m above the bottom, whichever was shallower. Each station included a rosette-CTD cast using a rosette from the Raytheon Polar Service Company (RPSC) and/or a Trace Metal Clean (TMC) rosette-CTD cast using a rosette from the University of Hawaii (Measures et al., 2008). Temperature, salinity and oxygen measurements were sampled during each RPSC and TMC cast using a SBE911 CTD and a SBE42 oxygen sensor. In addition, samples for measuring phosphate, nitrate and silicate concentrations were taken from bottles mounted on each rosette, with 12 bottles per cast.

The 2004 NOAA-AMLR survey performed 91 CTD casts during Leg 1 (January-February) and 98 casts during Leg 2 (February-March), using a Sea-Bird CTD mounted on a rosette equipped with 11 Niskin bottles. Nutrients were sampled only during Leg 1. Lipsky (2004) provides a full description of the instruments and methods used by the survey.

Two sets of CTD sensors were mounted on the RPSC rosettes and compared against each other at the beginning and end of the cruise in order to check for sensor drift. One set of sensors was used on the TMC rosette during LMG0402 and compared against the RPSC sensors. Because the thermocline waters in the study region are subject to high temporal variability, comparisons of RPSC vs. TMC sensors were done only for the 24 stations for which RPSC and TMC casts were performed within four hours of each other, and where the casts reached a depth of at least 1000 m. All sensor pair comparisons showed temperature differences within 0.01°C and salinity differences within 0.01 ppt. (Zhou et al., 2010a).

In addition to the CTD casts, 36 expendable CTDs (XCTDs) were dropped during NBP0606. However, the results of OMP analysis performed with combined CTD and XCTD data may have been affected by instrument bias, as discussed in Section 2.6.1.

Iron concentrations were determined from water samples taken with the TMC rosette at locations indicated by the shaded circles in Figure 2.2. The concentrations were determined using the flow injection analysis method (Measures et al., 1995). The

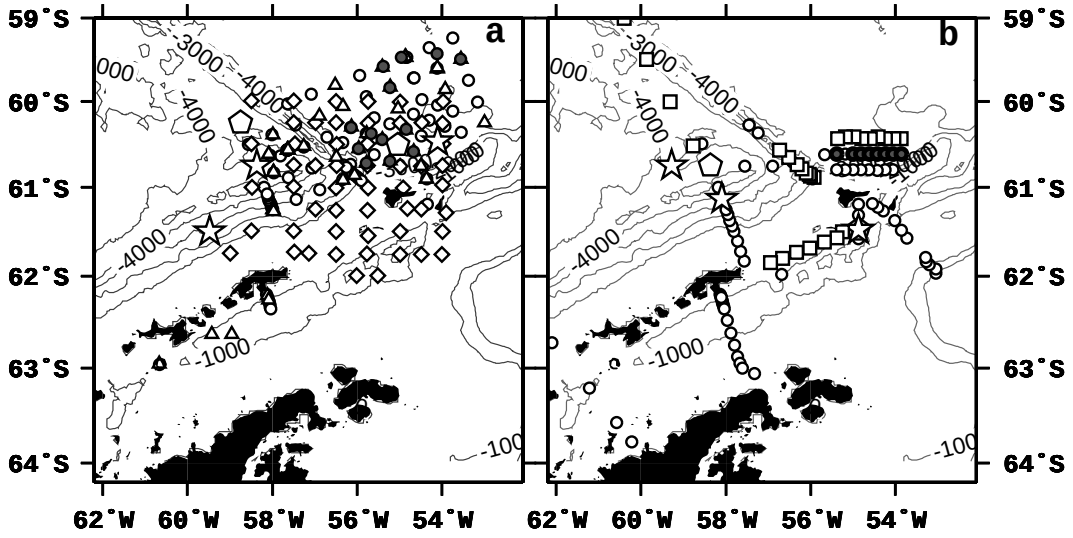

Figure 2.2: Station locations and source water points for (a) the LMG0402 and AMLR and (b) NBP0606 cruises. In (a), circles represent LMG0402 CTD stations, triangles represent TMC stations and diamonds represent AMLR CTD stations. In (b), circles represent CTD stations and squares represent XCTD casts. In both panels, stars identify the stations used as source points for the three-source scenario in the OMP analysis and pentagons mark the source points for the two-source scenario. Grey circles mark stations where iron was sampled.

iron concentration for the LMG0402 samples were subsequently reprocessed using inductively coupled plasma mass spectrometry (ICP-MS) (Houk and Thompson, 1988). The samples for NBP0606 are currently being reprocessed. Only a limited amount of data was obtained in the ACC waters with the lowest iron concentrations during LMG0402. Furthermore, iron was not measured during the 2004 NOAA-AMLR survey. In this study, we use the iron profiles to identify a density range corresponding to the subsurface iron peak but, since the iron data are sparse, we do not use iron as a parameter in the OMP analysis. However, other water properties, such as temperature, salinity, oxygen and nutrients, can be used to analyze the distribution of waters originating on the Antarctic shelf, (Hewes et al., 2008), which are known to be high in iron throughout the region (Hewes et al., 2008; Ardelan et al., 2010).

The oxygen concentrations measured by the RPSC sensors during LMG0402 and NBP0606 were calibrated by using Winkler titration oxygens from selected rosette bottles. Potential density for each titration was calculated from the CTD data at the depth of the bottle closures, and oxygen values from the titrations were compared against the sensor readings at matching densities during the downcasts. Oxygen samples were not drawn from the bottles mounted on the TMC rosette, so the TMC oxygens were calibrated using only the stations where titrations from an RPSC cast were available for the same location. The AMLR oxygen concentrations were not calibrated on board ship, since no titrations were conducted during the survey.

2.3 Optimal Multiparameter Analysis

2.3.1 The method

Optimal Multiparameter analysis was introduced by Tomczak and Large (1989). It is an extension of the multiparameter method originally developed by Tomczak (1981), which in itself is an extension of temperature-salinity diagram analysis. The method allows for the use of hydrographic properties other than temperature and salinity to

determine quantitatively the mixing ratios of n water types from a system of m linear equations. It has been used to evaluate water mass properties both in the Southern Ocean (Budillon et al., 2003; Tomczak and Liefrink, 2005) and in other regions, (e.g Tomczak and Large, 1989; Tomczak and Poole, 1999). This section provides a brief summary of the method.

Consider a situation in which n source waters contribute to a mixture of water observed at a hydrographic station. Assume the existence of a minimum of $m - 1$ oceanic parameters (such as temperature, salinity or oxygen), where $m > n$. The values of these parameters are measured both for the source water end point stations and for the other hydrographic stations. Water properties are assumed to be conserved during mixing. An additional mass balance constraint is created by requiring that some mixture of the source waters fully describe the water at the point of observation. The relative contributions of the n source waters at the observation point can then be represented by the linear system of conservation equations

$$\mathbf{Gx} - \mathbf{d} = \mathbf{r}, \tag{2.1}$$

where $\mathbf{G}$ is an $m \times n$ matrix containing the parameter values for the source waters, $\mathbf{d}$ is an n-element vector containing the observed parameter values for the mixed water, $\mathbf{x}$ is an m-element vector containing the relative contributions of the source waters to the mixing, and $\mathbf{r}$ is the n-element residual vector. The last line of $\mathbf{G}$ and the last element of $\mathbf{d}$ are set to 1 to represent the mass balance constraint. Traditionally, this final constraint is used as a measure of the uncertainty of the result, with mass balance residuals of 0.05 or less considered acceptable (Budillon et al., 2003; Tomczak and Large, 1989; Tomczak and Poole, 1999; Tomczak, 1981) The system is solved as an overdetermined least squares problem, minimizing $\mathbf{r}^T\mathbf{r}$, subject to the constraint that all elements of $\mathbf{x}$ must be nonnegative.

Before the system of equations in 2.1 can be solved, the values in $\mathbf{G}$ must be normalized in order to make parameters of different units comparable. We follow

Karstensen and Tomczak's (2005) method of computing the normalized matrix $\mathbf{G}'$ where

$$G'_{ij} = (G_{ij} - \overline{G_j})/\sigma_j, \tag{2.2}$$

where G_{ij} is the value of parameter j for source water i, G'_{ij} is the normalized value, $\overline{G_j}$ is the mean value of the parameter, and σ_j is the standard deviation.

In order to account for the biogeochemical changes in the source waters, we followed Karstensen and Tomczak's (1998) extension of the original OMP method by adding another column $r_{para}\Delta P$ to the left-hand side of Equation 2.1. The new column contains the Redfield ratios (Redfield et al., 1963) for oxygen, nitrate, phosphate and silicate, multiplied by the new unknown variable ΔP representing the change in phosphate (Karstensen and Tomczak, 2005). For temperature, salinity and mass balance, corresponding elements in the new column are set to 0. Equation (2.1) can then be rewritten as

$$\mathbf{G}_{ext}\mathbf{x}' - \mathbf{d} = \mathbf{r}, \tag{2.3}$$

where $\mathbf{G}_{ext} = [\mathbf{G}\ \mathbf{r}_{para}]$ and $\mathbf{x}' = [\mathbf{x}\ \Delta P]^T$.

Hoppema and Goeyens's (1999) analysis in the western Weddell Sea indicated that the canonical Redfield ratios of 16:1:138 for N:P:O_2 apply in Antarctic surface waters. Silva et al. (1995) showed similar mean values for the N:P ratio in the waters around Elephant Island, but found that mean Si:P values varied from 23:1 to 43:1, depending on depth and region of observation. Our own calculations, based on averaging the ratios for stations within the Ona Basin, produced Si:N:P:O of 29:15:1:156 for LMG0402 and 41:18:1:184 for NBP0606. The results discussed in Section 3 are based on our calculated ratios for each cruise. Replacing the O and N ratio with canonical Redfield values produced no statistically significant differences in the source water distributions.

Due to variations in measurement accuracy and spatial and temporal variability of the observed parameter values, a diagonal weight matrix $\mathbf{W}$ of dimension $m \times m$ is introduced. The full solution of the OMP analysis is then found by minimizing

$$(\mathbf{G}_{ext}\mathbf{x}' - \mathbf{d})^T\mathbf{W}^T\mathbf{W}(\mathbf{G}_{ext}\mathbf{x}' - \mathbf{d}) = \mathbf{r}^T\mathbf{r}. \tag{2.4}$$

2.3.2 Determining the weights

In OMP analysis, the weight matrix **W** is usually constructed so that the mass balance equation is assigned the highest weight among all the property conservation equations, and the mass balance residuals provide an objective indicator of the quality of the solution (Tomczak, 1981). In an ideal case, in which there is no measurement error, and the source waters specified in the input matrix **G** fully represent all of the waters that have been mixed to form the water at a given station, the last element of **r** would be equal to zero. Stations with high mass residuals may have water from other sources contributing to the mixing, or may be subject to non-linear processes that are not well-described by the linear model used in OMP analysis. Therefore, we follow Tomczak and Poole [1999] and focus our discussion on stations where the mass residuals are less than 0.05.

To obtain **W** for our analysis, we adapted the method originally described by Tomczak and Large (1989), which is based on relating the variance of each input parameter among the source waters to the variance of the same parameter within each source water. We define σ_j as a measure of how well parameter j is able to resolve the differences among n water masses:

$$\sigma_j = \sqrt{\frac{1}{n}\sum_{i=1}^{n}(G_{ij} - \bar{G_j})^2}, \tag{2.5}$$

where G_{ij} represents the element of G corresponding to the value of parameter j in water mass i, and $\bar{G_j}$ is the mean value of parameter j at the end points.

We then calculated the source water variances δ_j using the TS-diagrams in Figure 2.6 to determine which stations were most likely sampled within the same source water. We computed the mean value of each parameter for each group of stations within

Table 2.1: Weights used for OMP analysis in summer 2004 (LMG0402) and winter 2006 (NBP0606).

	3-source		2-source	
Parameter	LMG0402	NBP0606	LMG0402	NBP0606
Temperature	10	10	9	9
Salinity	10	11	7	13
Oxygen	7	25	7	15
Phosphate	16	4	2	2
Nitrate	8	3	6	3
Silicate	17	4	2	1
Pot. Vorticity	11	19	19	14

the layer where the analysis was to be performed, and computed the variance of the means. The largest of the δ_j values among our n source waters is defined as δ_{jmax}. The weights are then calculated as

$$W_j = \sigma_j^2/\delta_{jmax}. \tag{2.6}$$

The weights computed for each parameter from the resulting variances are summarized in Table 2.1. Since OMP does not provide a straightforward method for assigning weights to the mass balance equation, which is not based on any measurements (Tomczak and Large, 1989; de Brauwere et al., 2007), we followed the usual practice (Tomczak and Large, 1989; You and Tomczak, 1993) and assigned the largest of our calculated weights to the mass balance. As an alternative method, we also performed our analysis with weights based on the inverse variances of individual parameter measurements, as is typically done for least-squares fitting methods. While distributions at individual stations were affected by the resulting changes in weights, the resulting spatial distributions of SWT percentages and mass balance residuals remained consistent with the conclusions we present in Section 2.6. We selected Tomczak and Large's (1989) method as being more physically meaningful, since it takes into account the variability of properties among the different water masses as well as the variability within each mass.

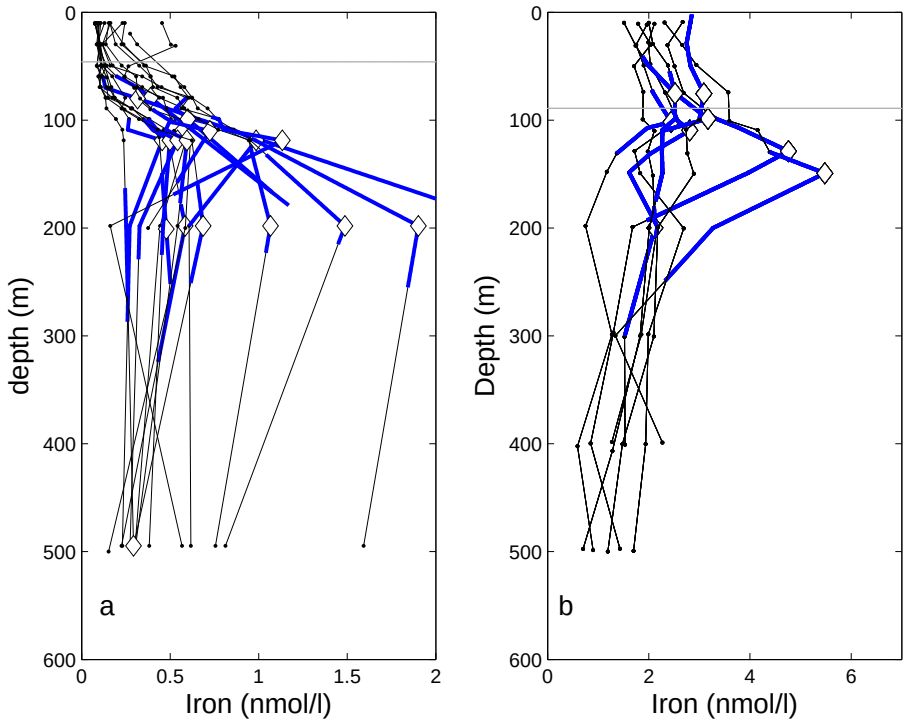

Figure 2.3: Profiles of Iron in the Ona Basin for (a) March 2004 (LMG0402) and (b) August 2006 (NBP0606). Gray horizontal lines indicate typical mixed layer depth as determined by Dong et al. (2008), and segments shaded in blue indicate the maximum and minimum depth of the 27.5$\leq \sigma_\theta \leq$27.6 density layer. Diamonds indicate the iron maximum at each individual station.

2.4 Iron distribution and selection of the density range for OMP analysis

Iron profiles for the stations sampled in the Ona Basin during LMG0402 and NBP0606 are shown in Figure 2.3. The iron concentrations for LMG0402 are significantly lower than for NBP0606 due to increased iron consumption by the phytoplankton during the summer. However, the profiles for both cruises consistently show iron concentrations increasing below 100 m and decreasing again below 200 m. The iron

maximum is below the mixed layer both in summer and in winter. To determine the density range where the maximum iron concentrations are located, we found the value of σ_θ at the peak depth for every station, then used the range between the maximum and minimum values of σ_θ, rounded to one decimal place, for our OMP analysis. This method produced a density range of $27.5 \leq \sigma_\theta \leq 27.6$ for both cruises. The thickness and median depth of these density layers are shown in the top rows of Figure 2.4 for LMG0402 and Figure 2.5 for NBP0606. The maximum and minimum depths of the layers are shown as blue horizontal lines in Figure 2.3. The thickness and depth of the density layer immediately below, where $27.6 \leq \sigma_\theta \leq 27.7$, are shown in the bottom rows of Figure 2.4 for LMG0402 and Figure 2.5 for NBP0606.

For both cruises, the two density layers are thicker in the deep waters to the west of the STR than the deep waters to the east. For LMG0402, both layers are thinnest over the continental shelf on both sides of the ridge, and become thicker away from the shelf. For NBP06, the layers are thinnest for shelf transects A and C (Figure 2.2 b), where the end point stations for SW1 and SW2 are defined.

2.5 Selecting source waters for OMP analysis

Optimal Multiparameter analysis, as developed by Tomczak and Large (1989), is based on the assumption that observed water properties at a hydrographic station are the result of mixing among two or more "source waters". Usually the source waters are assumed to be linear combinations of two or more sea water types (SWTs), whose physical and chemical properties are known (Tomczak and Large, 1989). The values of **G** are then determined by linear regression of all parameters against temperature. By limiting our analysis to a vertically narrow isopycnal layer, we were able to define each of our source waters as a single SWT. This approach allowed us to determine the values of **G** directly from observations by taking measurements of each parameter at selected end point stations and averaging them vertically within the layer where the analysis would be performed. In this section, we discuss our selection of end point stations that

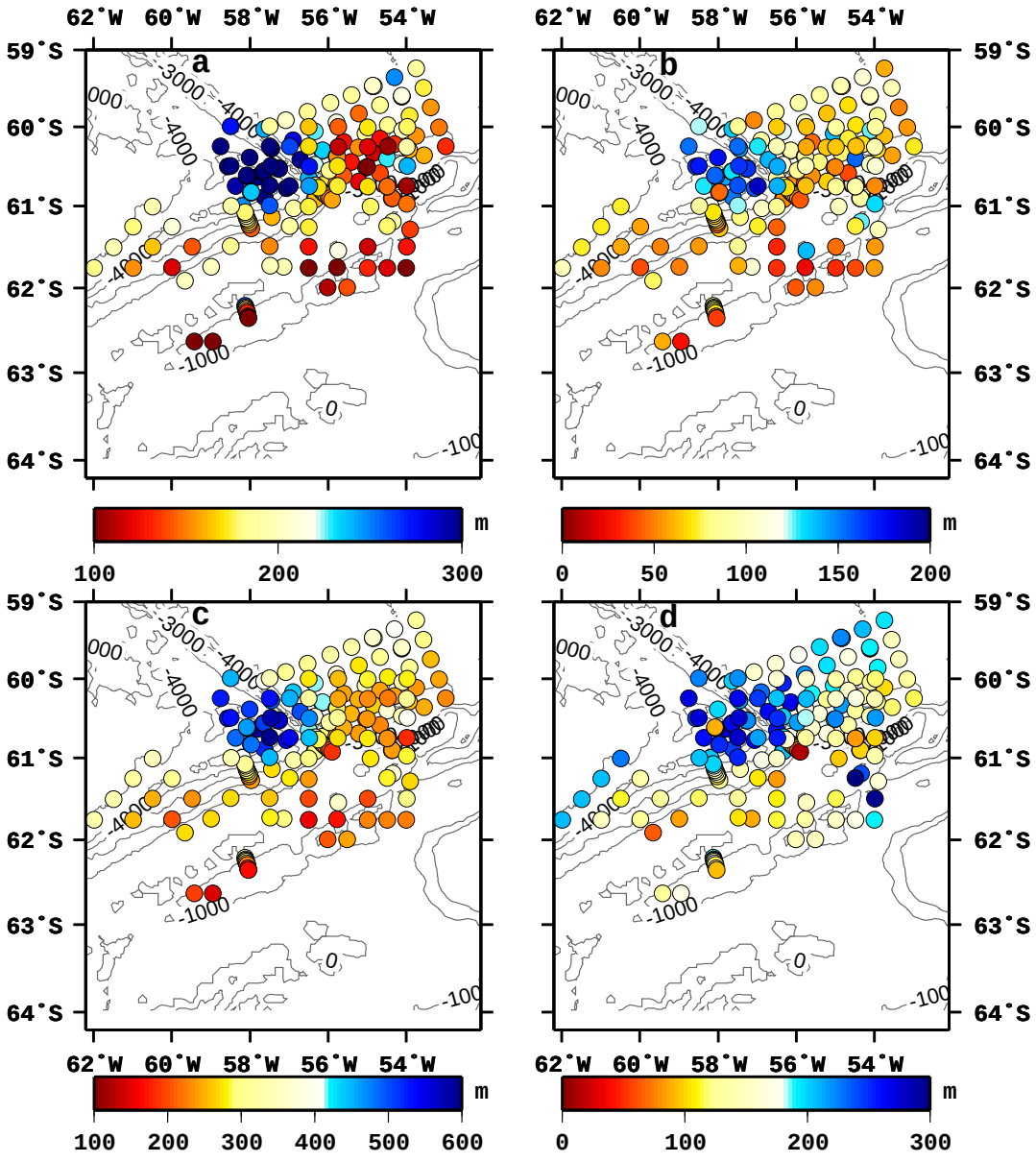

Figure 2.4: Top row: median depth (a) and thickness (b) of the 27.5$\leq \sigma_\theta \leq$27.6 density range containing the iron peak for LMG0402. Bottom row: median depth (c) and thickness (d) of the density range 27.6$\leq \sigma_\theta \leq$27.7

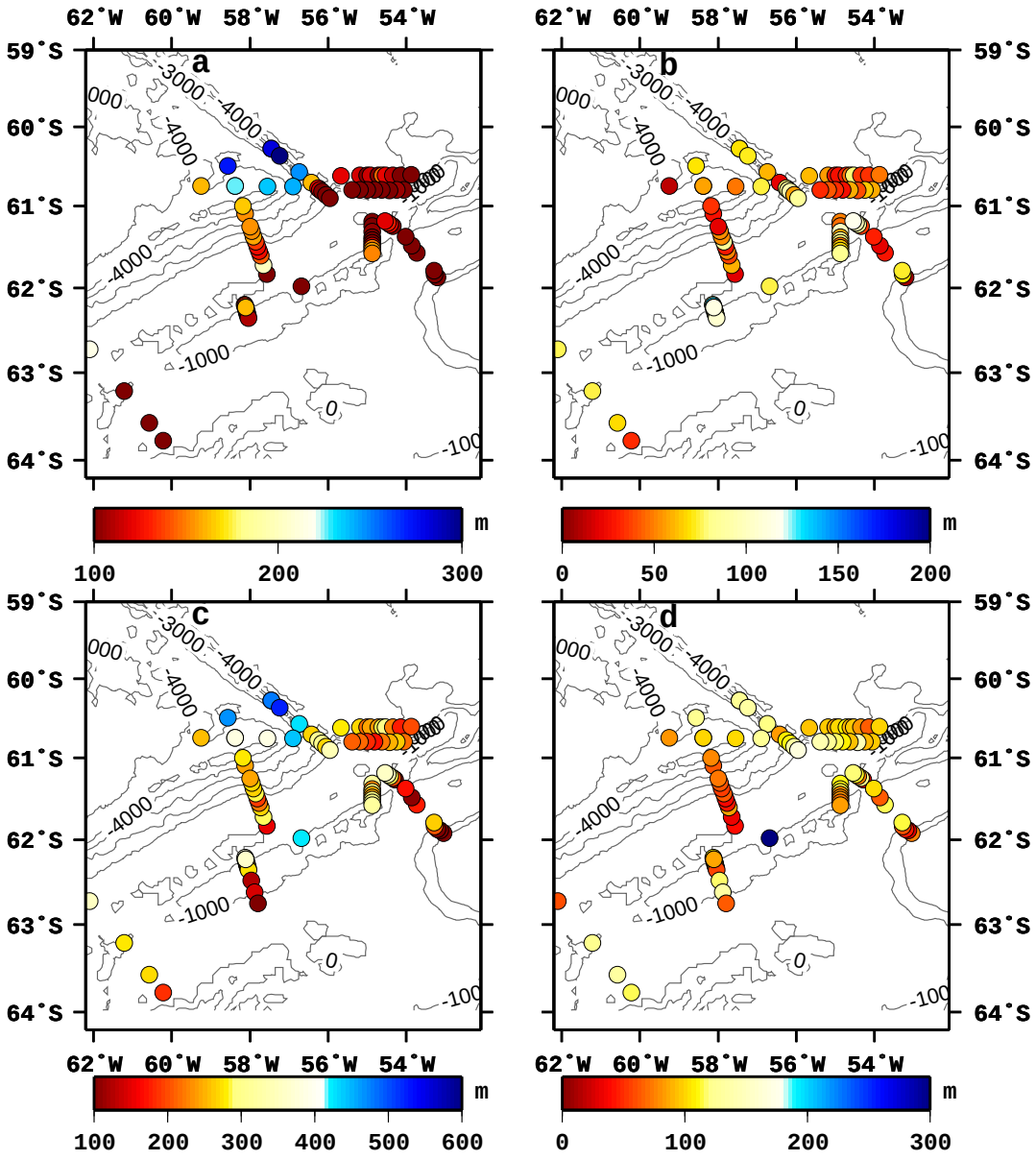

Figure 2.5: Top row: median depth (a) and thickness (b) of the 27.5$\leq \sigma_\theta \leq$27.6 density range containing the iron peak during NBP0606. Bottom row: median depth (c) and thickness (d) of the density range 27.6$\leq \sigma_\theta \leq$27.7

represent the source water properties to be used as inputs for our analysis.

Appropriate definition of source waters properties is crucial to achieving physically meaningful results from OMP. To identify the stations that best represent the source waters for our region, we compared the temperature-salinity (TS) profiles from the CTD casts in our data set against the characteristic TS properties of the water masses in Drake Passage (Whitworth et al., 1994; Hofmann et al., 1996; Zhou et al., 2010b). We considered potential end points in the ACC, the Bransfield Strait, and on the continental shelf, with additional consideration given to differences between the shelf waters to the east and west of the STR.

Figure 2.6 shows the TS profiles for stations used to select potential OMP end points for summer (Figure 2.6a) and winter (Figure 2.6b). Profiles plotted in red represent stations located north of the SACCF and east of the STR, where the ACC flow can be expected to dominate. All stations in both years show the typical CDW profile, with Upper Circumpolar Deep Water (UCDW) profile below the 27.2 isopycnal, consistent with previous sections across Drake Passage (Brandon et al., 2004). Above the 27.2 isopycnal, the LMG0402 stations show the warmer and slightly fresher Antarctic Surface Water (ASW) layer that is not present during NBP0606, as is consistent with surface warming during the summer months.

The shelf water profiles in Figure 2.6 are plotted in green for stations west of the STR, and blue for stations to the east. During LMG0402, the western stations fall into two distinct clusters. One cluster shows the characteristic CDW profile, closely overlapping with the ACC profiles above the 27.2 isopycnal, but becoming consistently colder than the ACC for σ_θ >27.2, consistent with local cooling of the CDW. The other cluster of colder, saltier shelf waters is consistent with the intrusion of BW into the shelf waters around the South Shetland Islands. However, the TS profiles in the second cluster could not be easily distinguished from the profiles east of the STR. For the NBP0606 profiles, the differences between the two clusters of the western shelf stations is less distinct, and the coldest of the western shelf stations once again show significant overlap in water properties with the eastern shelf stations.

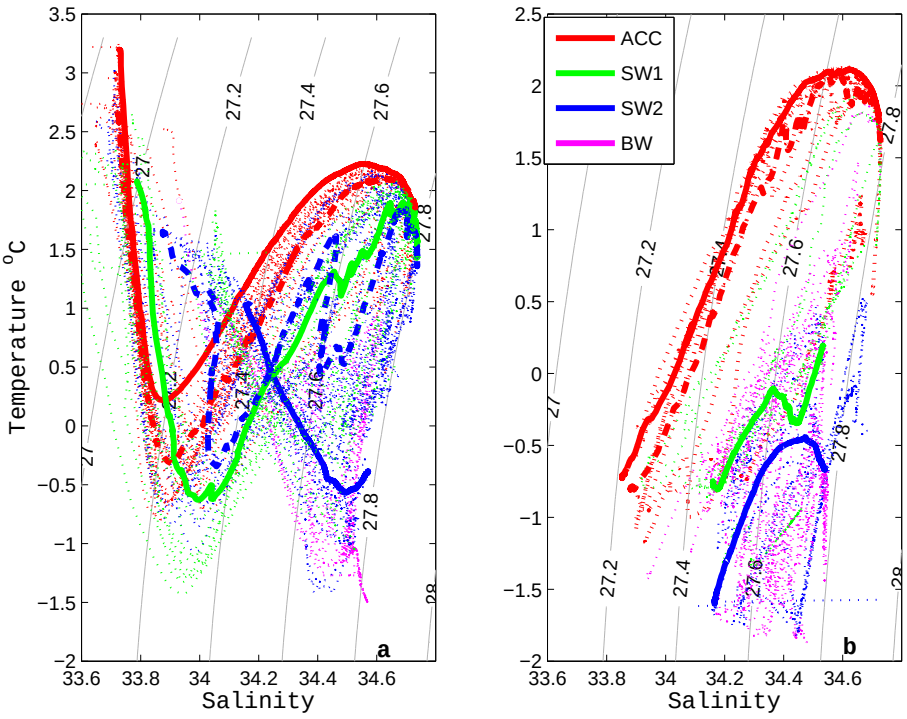

Figure 2.6: Temperature and salinity profiles for stations used to determine source water properties for OMP analysis. For the three-source scenario, solid red lines represent the stations chosen to represent the source waters for (a) LMG0402 and (b) NBP0606. Solid green lines represent the SW1 source water stations, and solid blue lines represent the SW2 stations. For the two-source scenarios, dashed lines represent the stations chosen for ACC and SW. During NB060, the same station was selected to represent SW2 and SW in both scenarios. Dotted lines in each color represent the other stations sampled within the same source water.

Profiles from the Bransfield Strait are plotted in magenta in Figure 2.6. For LMG0402, the BW profiles are similar to SW2, but with temperatures up to 0.5°C colder than SW2 in our chosen density range. During NBP0606, when the Bransfield Strait stations were sampled in a high-resolution transect across the entire strait, the TS profiles overlap with both SW1 and SW2, reflecting the difference in water properties between the northeastward flow of the Bransfield Current along the southern shelf of the South Shetland Islands and the southwestward countercurrent in the southern part of the strait (Hofmann et al., 1996; Zhou et al., 2002).

Temperature and salinity alone suggest two potential source waters for OMP analysis, one representing the ACC and one representing all shelf waters (SW) in the SFZ. However, OMP analysis allows for the inclusion of other parameters, such as nutrients, oxygen and potential vorticity, which may help distinguish waters that have similar TS properties but originate from different sources. While nutrient concentrations are affected by biogeochemical processes and cannot be assumed to be conserved during mixing, Karstensen and Tomczak's (1998) extension of the original OMP method accounts for these changes through the use of Redfield ratios, as explained in 2.3. The nutrient data allow us to make further distinction between the shelf waters to the east and west of the STR. We will refer to the SW on the western side of the STR as SW1, and to the SW on the eastern side as SW2. The additional parameters also allow us to test the suitability of BW as an additional source water, both as a potential fourth source and as a replacement for either SW1 or SW2 in a three-source scenario.

The potential vorticity (PV) for our analysis was computed as

$$PV = \frac{N^2 f}{g}, \tag{2.7}$$

where N is the buoyancy frequency, f is the Coriolis frequency, and g is the gravitational acceleration. As seen in Figures 2.4 and 2.5, the density layers covered in our analysis are thickest in the northwest portion of our sampling region, where the CDW TS properties dominate, and thinnest on the shelf. The resulting difference in potential

Table 2.2: Location of stations used to represent the source waters for OMP analysis for the two-source and three-source scenarios.

	LMG0402				
	3-source			2-source	
	ACC	SW1	SW2	ACC	SW
Latitude	-60.53	-61.2	-60.51	-60.25	-60.51
Longitude	-57.26	-58.03	-55.04	-58.7	-55.04
	NBP0606				
	3-source			2-source	
	ACC	SW1	SW2	ACC	SW
Latitude	-60.5	-61.61	-61.25	-60.75	-61.25
Longitude	-58.56	-57.73	-54.88	-58.37	-54.88

vorticity helps us to further distinguish the ACC waters from the shelf waters.

To select appropriate stations for defining our source waters, we defined a parameter space of seven dimensions: temperature, salinity, oxygen, phosphate, nitrate, silicate and PV. Each station was assigned a seven-element coordinate vector of these parameters, computed by vertically averaging the values over the $27.5 \leq \sigma_\theta \leq 27.6$ density layer. Each vector was then normalized following Karstensen and Tomczak's (2005) method as described in Equation 2.2 in 2.3. To ensure that the results of the OMP analysis most fully describe the water composition in our region, it is desirable to select stations whose property vectors most fully span our parameter space to represent our source waters. If using two source waters, this criterion can be satisfied by choosing two stations whose coordinate vectors place them farthest apart in the parameter space. If using three source waters, we can view their coordinates as points defining a triangle in the parameter space, and select the three stations whose coordinate vectors span the largest triangle area. By extension, an ideal four-source scenario would use four points defining a solid with maximum volume in the parameter space. However, preliminary tests with a four-source scenario showed that it did not represent the mixing in the region as well as a three-source scenario, and the possibility of a fourth source water was not explored in greater detail.

Table 2.3: Definitions of source water end points used for the three-source OMP analysis.

Source Water	T (°C)	S (ppt)	O_2 (μmol/kg)	PO_4 (μmol/kg)	$N0_3$ (μmol/kg)	Si (μmol/kg)	Pot. Vort.
27.5$\leq \sigma \leq$27.6 LMG0402+AMLR							
ACC	1.84	34.46	189	2.4	35.1	54.5	0.095
SW1	1.56	34.44	228	2.7	51.4	115.3	0.1
SW2	1.37	34.42	208	2.2	33.1	69.1	0.21
27.6$\leq \sigma \leq$27.7 isopycnal, LMG0402+AMLR							
ACC	2.08	34.61	171	2.4	34.6	74.9	0.06
SW1	1.80	34.59	175	2.3	34.3	70.3	0.10
SW2	1.33	34.54	191	2.3	34.7	75.3	0.08
27.5$\leq \sigma \leq$27.6, NBP0606							
ACC	0.81	34.38	217	1.9	31.8	71.7	-0.18
SW1	0.49	34.36	297	1.9	33.9	75.7	-0.88
SW2	-.55	34.26	288	1.7	32.6	77.2	0.06
27.6$\leq \sigma \leq$27.7 isopycnal, NBP0606							
ACC	2.07	34.61	173	2.2	34.6	79.2	0.07
SW1	-0.25	34.43	264	2.0	31.2	75.4	0.08
SW2	-0.37	34.42	265	1.8	35.0	87.3	-0.02

The locations of the source water stations selected for the two-source and three-source scenarios are shown in Table 2.2. The profiles for these stations are plotted as solid and dashed lines in Figure 2.6, and their averaged water properties in our chosen density range are summarized in Tables 2.3 and 2.4.

2.5.1 Sensitivity analysis

To obtain a quantitative measure of the robustness of our computed source water distributions, we examined the sensitivity of our results to random variations in the source water definitions. A total of 100 iterations of a Monte Carlo simulation were performed. For each iteration, random perturbations for each parameter – temperature,

Table 2.4: Definitions of source water end points used for the two-source OMP analysis.

Source Water	T (°C)	S (ppt)	O_2 (μmol/kg)	PO_4 (μmol/kg)	$N0_3$ (μmol/kg)	Si (μmol/kg)	Pot. Vort.
27.5$\leq \sigma \leq$27.6 LMG0402+AMLR							
ACC	1.80	34.45	189	2.2	31.9	54.5	0.10
SW	1.37	34.42	208	2.2	33.1	69.1	0.22
27.6$\leq \sigma \leq$27.7 isopycnal, LMG0402+AMLR							
ACC	2.08	34.61	171	2.4	34.6	74.9	0.06
SW	2.03	34.62	198	2.4	44.3	93.6	0.06
27.5$\leq \sigma \leq$27.6, NBP0606							
ACC	1.69	34.45	189	2.2	37.7	64.8	0.11
SW	-1.24	34.23	316	1.9	26.1	77.9	0.13
27.6$\leq \sigma \leq$27.7 isopycnal, NBP0606							
ACC	2.00	34.60	173	2.2	30.0	74.1	-0.79
SW	-0.53	34.42	276	1.8	34.6	77.3	0.09

salinity, oxygen and nutrients – were generated from a zero-mean Gaussian distribution with the same standard deviation as the measured parameter within each source water. A standard deviation of the difference between the simulated scenarios and the unperturbed scenario was computed for the fractional contribution from each source water at every station, as well as a mean standard deviation for the entire region. Standard deviations for the mass residuals at each station were also computed. The results of this analysis are discussed in section 2.6.2

As an alternative sensitivity estimate, we also examined the standard deviations of each source water distribution within the isopycnal layer prior to averaging. The resulting sensitivity values (not shown) were smaller than the values given by the Monte Carlo method for 85% of all stations. Since this estimate does not account for measurement bias or for the high degree of correlation likely to exist for vertically adjacent points within an isopycnal, we chose the Monte Carlo method as a more complete measure of the sensitivity of our results.

2.6 Results and discussion

2.6.1 Source water distribution in the iron peak density range

We performed the OMP analysis for every station and averaged the resulting source water contributions vertically for the density range illustrated in the top row panels of Figures 2.4 and 2.5. The source water distributions were computed twice, once each for the two-source and three-source scenarios. In order to make a meaningful comparison of the scenarios, we calculated a chi-square (χ^2) estimator (Press et al., 1986) for the standard deviation of individual parameters at all stations, and computed the probability of exceeding a given χ^2 value with random data. The details of the method are given in Appendix A.

The resulting source water distribution for individual LMG0402 and AMLR stations is illustrated by the pie charts in Figure 2.7a for the three-source scenario and Figure 2.7b for the two-source scenario. The distributions for NBP0606 are shown in Figure 2.7c and d. Upstream of the STR, where the density layer is thickest, the distributions for both summer and winter show the ACC water as the dominant water mass in the region, with little or no shelf water present in the stations north of the 2500 m bathymetry contour. This part of the region is also characterized by low iron (Martin et al., 1990; Hewes et al., 2008; Ardelan et al., 2010) and low Chl-a (Figure 2.1b). Downstream of the STR, where the Chl-a levels are elevated, shelf waters dominate the water composition, with 60% of LMG0402 stations, 67% of NBP0606 CTD stations, and 60% of combined NBP0606 CTD and XCTD stations east of the STR showing ACC contributions of less than 5%. This distribution is consistent with Zhou et al.'s (2010a) conclusion that the ACC flow east of the STR is redirected to the northeast by conservation of potential vorticity. The two-source and three-source distributions for both summer and winter show both SW1 and SW2 present upstream and downstream of the STR, with SW1 properties dominating. The χ^2 estimator test indicates a probability difference of less than 0.5% between the two-source and three-source scenarios,

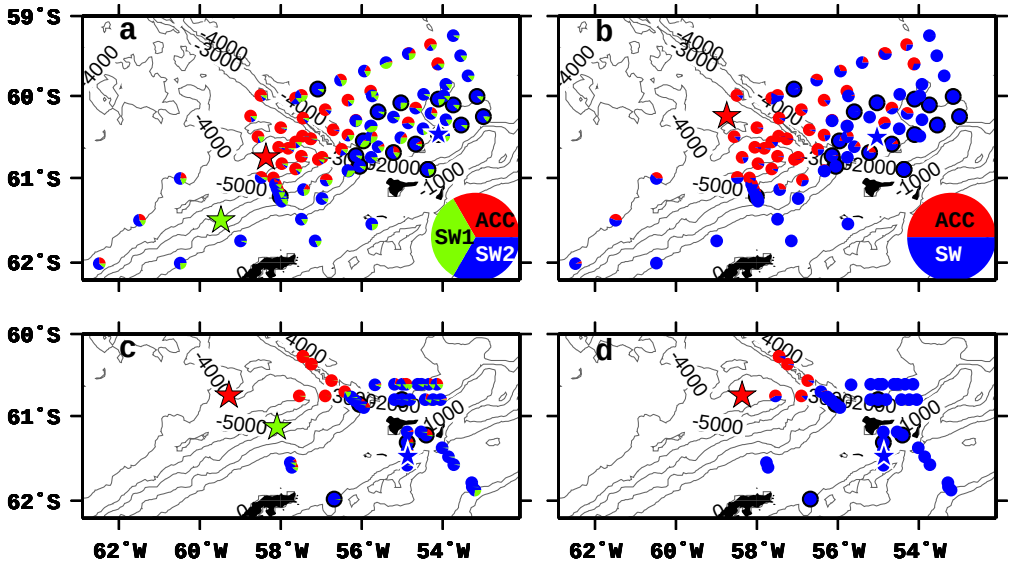

Figure 2.7: Source water distributions along the 27.5$\leq \sigma_\theta \leq$27.6 isopycnal computed with OMP analysis during LMG0402 (a and b) and NBP0606 (c and d). The pie charts show station locations, and stars show the locations of source point stations. The source waters for the three-source scenario (a and c) are ACC water (ACC), Shelf Water 1 (SW1), and Shelf Water 2 (SW2). The source waters for the two-source scenario (b and d) are ACC and Shelf Water (SW). Pie charts circled in black represent stations where Monte Carlo analysis produced a root-mean-square difference of more than 0.05 from the unperturbed case.

and the ACC contributions between the two scenarios showed no statistically significant changes, with differences at all stations being smaller than the standard deviations computed in our sensitivity analysis. The similarity between the two scenarios suggests intermixing among shelf waters in the sampling region, with Weddell Sea waters influencing the hydrographic properties at all shelf stations. Such mixing is consistent with past hydrographic (Niiler et al., 1991; von Gyldenfeldt et al., 2002) and drifter (Zhou et al., 2002) studies, which indicate that some northward-flowing Weddell Sea waters turn southwestward at the tip of the Antarctic Peninsula and intrude into the Bransfield Strait and the shelf break around the South Shetland Islands.

The distributions for the three-source scenarios that included BW as a source point (not shown) were nearly identical to the three-source distribution shown in Figure 2.7, with BW replacing SW1. However, both the sensitivity analysis described in Section 2.5.1 and the χ^2 estimator computed following the method in Appendix A indicate that the waters in the Ona Basin are more accurately represented as a combination of ACC and shelf waters only, with BW affecting the circulation primarily through its influence on the shelf waters west of the STR.

Distribution of water properties in the ocean is affected both by stirring, which redistributes properties through advection while maintaining gradients, and by mixing, which decreases the gradients through diffusion (Eckart, 1948). Abraham et al. (2000) have demonstrated the importance of horizontal stirring in the development and sustainment of an iron-fertilized bloom. The OMP-derived distributions in Figure 2.7 shows that within the Ona Basin, in the central part of our study region, the water composition varies from station to station. Adjacent stations are frequently dominated by different source waters. Using Argo data, Barré et al. (2008) found similar patchiness of potential temperature, salinity and σ_θ distributions in the same region. Such variable distribution near the ridge is consistent with a filamented structure that could be caused by advective stirring. Farther downstream, the easternmost LMG0402 stations show a more uniformly mixed water composition dominated by a mixture of SW2 and SW1, suggesting that the waters are retained within the basin long enough for the stirring to

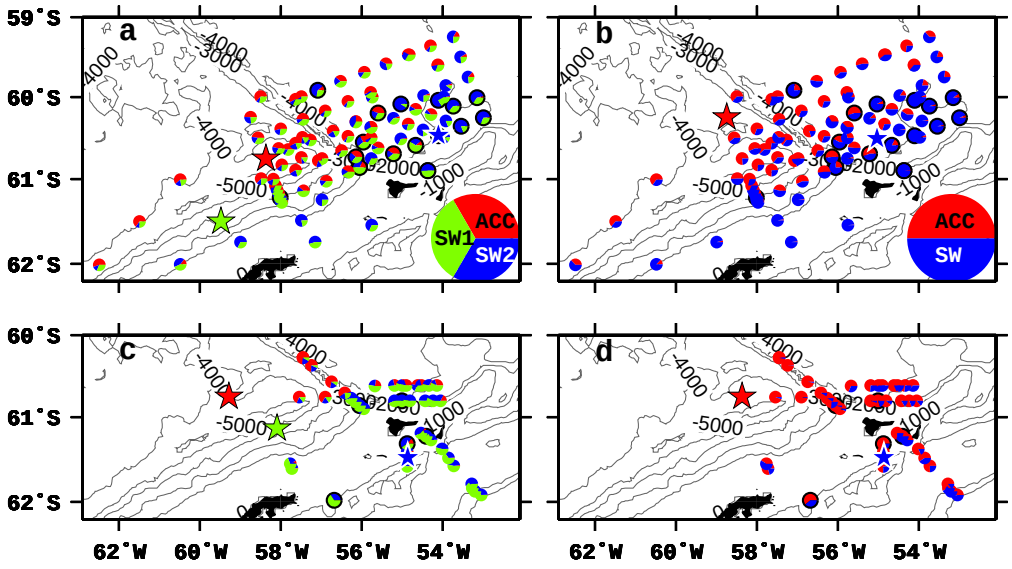

Figure 2.8: Source water distributions along the 27.6$\leq \sigma_\theta \leq$27.7 isopycnal computed with OMP analysis using only CTD stations during LMG0402 (a and b) and NBP0606 (c and d). Symbols and colors are as in Figure 2.8.

lead to mixing, homogenizing the water properties as the water advects downstream. Such a scenario is consistent with Argo floats becoming trapped in the basin for periods ranging from 6 to 20 months between 2002 and 2006 (Barré et al., 2008). For NBP0606, the stations at the eastern edge of the study region are too few and too closely spaced to determine if homogenized mixing has taken place.

The source water distributions along the 27.6$\leq \sigma_\theta \leq$27.7 density layer are shown in Figure 2.8. These distributions were calculated using the same end point station locations as the iron peak layer. For the three-source scenario, the distributions for NBP0606 (panel c) are largely the same as in the iron maximum layer, with a slightly greater presence of SW1 in the Ona Basin, and ACC water still dominant west of the STR. The LMG0402 distribution (panel a) shows a smaller presence of ACC water

throughout the region, but retains the filamented distribution in the Ona Basin with homogenized mixing in the east. Distributions computed with endpoints optimized for the $27.6 \leq \sigma_\theta \leq 27.7$ layer (not shown) slightly increase the ACC concentrations west of the STR, but do not significantly affect the results for the Ona Basin. The two-source distribution for LMG0402 (panel b) is similar to the distribution for the $27.5 \leq \sigma_\theta \leq 27.6$ density layer, while the two-source distribution for NBP0606 (panel d) shows a higher proportion of ACC waters, especially for stations where SW1 is dominant in the three-source scenario, suggesting a stronger winter influence of CDW in this density range on the shelf waters west of the STR.

While the winter distributions shown in Figures 2.7 and 2.8 are consistent with the summer distribution in showing the increased presence of shelf waters in the Ona Basin compared to the ACC-dominated waters to the west of the STR, the CTD casts during NBP0606 did not sample far enough off-shore to determine if the filamented distribution seen in the summer months is still present in winter. To extend the spatial coverage for the winter analysis, we performed the OMP analysis with a combination of CTD and XCTD data, using temperature, salinity and potential vorticity as the input parameters. The results, illustrated in Figure 2.9, showed increased presence of SW1 throughout the sampling region. However, comparison of temperature profiles (Figure 2.10) indicated a possible warm bias in XCTD measurements compared to CTD, which may have affected the outcome of the analysis.

2.6.2 Sensitivity of the results

The spatially averaged results of the Monte Carlo sensitivity analysis for the entire study region are summarized in Table 2.5. Individual stations for which the average root-mean-square difference between the Monte Carlo simulation and the unperturbed scenario exceeded 0.05 for any source water are indicated by black circles around the pie charts in Figures 2.7 and 2.8. In both years, the stations with the highest sensitivity to small perturbations in source water definitions tend to be clustered near or on the shelf in

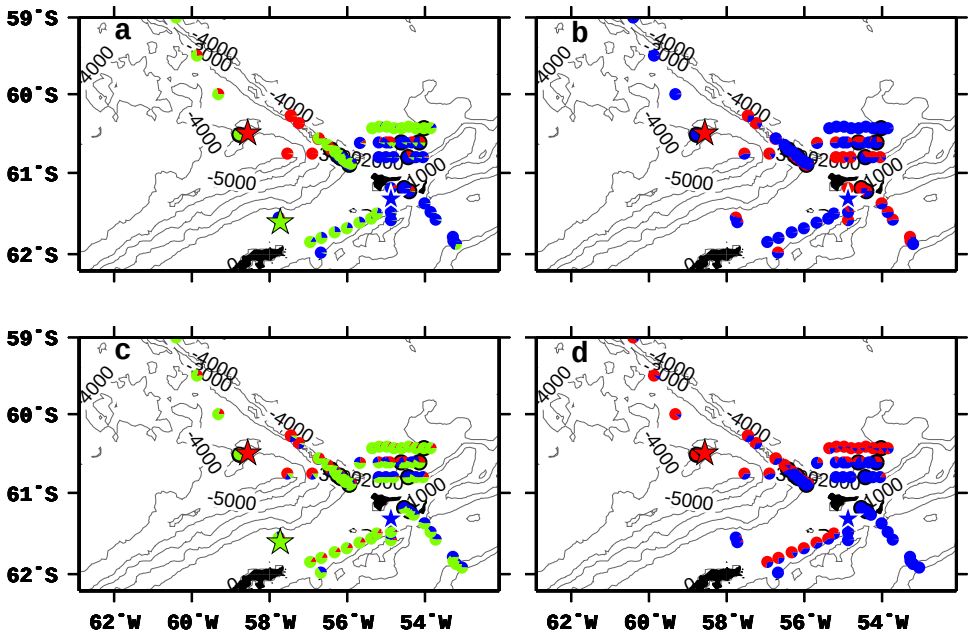

Figure 2.9: Source water distributions computed with OMP analysis using combined CTD and XCTD data during NBP0606 for the three source (panels a and c) and two-source (panels b and d) scenarios. Symbols and colors are as in Figure 2.8. Panels a and b represent the 27.5$\leq \sigma_\theta \leq$27.6 isopycnal, and panels c and d show the 27.6$\leq \sigma_\theta \leq$27.7 isopycnal.

Table 2.5: Spatially averaged standard deviations of source water distributions, computed from a 100-iteration Monte Carlo simulation. The original distributions are given as percentage contributions of each source water to the total mixing at each station, and the percentages in the table represent absolute deviations from the unperturbed case.

	LMG0402+AMLR		NBP0606	
Source Water	27.5$\leq \sigma \leq$27.6 Isopycnal	27.6$\leq \sigma \leq$27.7 Isopycnal	27.5$\leq \sigma \leq$27.6 Isopycnal	27.6$\leq \sigma \leq$27.7 Isopycnal
ACC	2.2%	1.8%	5.0%	3.9%
SW1	2.9%	5.1%	3.4%	5.0%
SW2	1.7%	4.5%	4.0%	4.8%

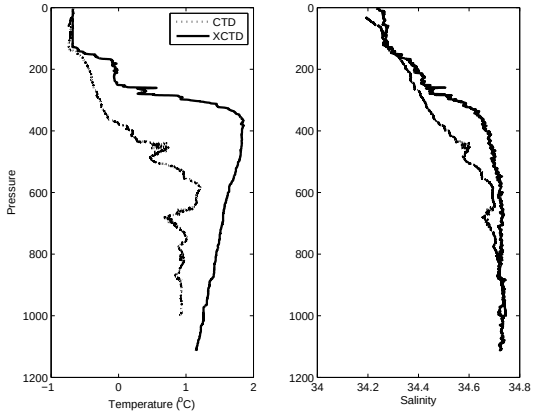

Figure 2.10: Temperature and salinity profiles sampled by CTD and XCTD at -56.3°W and -60.8°S

the eastern part of the study region. The most sensitive stations are the ones dominated by mixing between SW1 and SW2, while those where ACC water dominates show the lowest standard deviations. For both cruises, the ACC water contributions throughout the region were less sensitive than the shelf water distributions.

Overall, the OMP results for NBP0606 were more sensitive to small perturbations than the LMG0402 and AMLR results. The differences may be caused by seasonal variations, or by the different sampling patterns between the summer and winter surveys. Most NBP0606 stations were located over relatively shallow topography in the southeastern part of the study region, where the LMG0402 and AMLR stations also showed higher sensitivities.

2.7 Summary

In this study, we have used CTD data from multiple surveys to perform an OMP analysis of the source water distribution in the southern Drake Passage during the summer of 2004 and the winter of 2006. The extended version of the OMP analysis was used, incorporating Redfield ratios to partially account for the biogeochemical changes.

The results give us the means to assess the horizontal distribution of iron-rich shelf waters in our study region.

Adjacent stations near the STR in the Ona Basin show very different source water compositions, consistent with a filamented distribution created by advective stirring. Farther downstream, the source water distribution becomes more uniform, suggesting that the waters in the basin are retained long enough for the stirring to eventually lead to homogeneous mixing. Satellite-derived Chl-a images (Kahru et al., 2007) also demonstrate filamentation, with adjacent strands of high and low Chl-a found in eddies and frontal zones.

While the shelf waters near the South Shetland Islands are geographically separated from the shelf waters near the Weddell Sea (Hofmann et al., 1996; Zhou et al., 2010b), treating the two as separate shelf water sources did not produce statistically significant improvements in either the χ^2 estimator or the sensitivities computed from the Monte Carlo simulation described in Section 2.5.1. The similarity between the results of the two-source and three-source scenarios suggests that the shelf waters are not sufficiently distinct in their TS and nutrient properties to justify treating them as separate source waters for the purposes of our analysis. By contrast, the χ^2 and sensitivity results for scenarios that include the Bransfield Strait indicate that BW does not directly contribute to the mixing in the Ona Basin but instead influences the source water distributions in the basin only indirectly, thorough its influence on the shelf waters.

The distributions shown in Figures 2.7 and 2.8 indicate that in the density range where iron concentration is highest, shelf waters from both east and west of the STR flow into the Ona Basin. Previous studies of circulation in the region (Brandon et al., 2004; Barré et al., 2008) indicate the presence of persistent deep mesoscale eddies that trap water in the basin. In Barré et al.'s (2008) study, Argo floats released in March 2002 and December 2003 remained in the basin for periods ranging from six months to two and a half years. Such long retention times, combined with the offshore advection suggested by our analysis, would allow for a build up of high iron concentrations below the mixed layer in the Ona Basin. Drake Passage is a region of enhanced vertical mixing in the

upper ocean (e.g. Thompson et al. (2007)), which facilitates iron diffusion from the top of the thermocline into the mixed layer. It is also a region of high seasonal variability in mixed-layer depth (Dong et al. (2008); Figure 2.3), facilitating entrainment of iron toward the surface as the mixed layer deepens during late summer and fall. Such a combination of horizontal and vertical processes is consistent with the hypothesis that the northward flow of these shelf waters supplies the iron that enhances the biological productivity in the Ona Basin.

Chapter 3

An assessment of the accuracy of fine-scale methods for estimating mixing

3.1 Introduction

Diapycnal turbulent mixing is a dominant factor in controlling the stratification and energy budget of the global ocean, as well as vertical fluxes of fresh water, nutrients and dissolved tracers. In the upper ocean, it drives the heat and gas exchanges between the ocean and the atmosphere, affecting the ocean's role in regulating global climate. Early theory, based on the assumption of uniform mixing throughout the global ocean, estimated mean global diapycnal diffusivity κ to be on the order of 10^{-4} m^2s^{-1} (Munk, 1966). However, subsequent observations revealed a high degree of spatial variability, with typical background diffusivities of 10^{-5} m^2s^{-1} and regions of intense mixing, where κ could be as high as 10^{-3} m^2s^{-1} (Gregg, 1987; Toole et al., 1994).

The typical vertical length scales for diapycnal mixing are on the order of a few centimeters. Such small scales can be directly resolved with microstructure measurements, but the availability of these measurements is limited due to cost, need for trained

personnel, and difficulty of deploying the instruments in rough weather conditions. As a result, a number of alternative methods of estimating κ from fine-scale measurements have been developed. Methods based on detecting static instabilities in otherwise stably stratified density profiles (Thorpe, 1977; Dillon, 1982) and on parameterizations of internal wave shear and strain variances (Kunze, 2003) have been applied to a wide range of observations made with CTDs (e.g. Sloyan (2005), Kunze et al. (2006), Gargett and Garner (2008)), XCTDs (e.g. Thompson et al. (2007)) and lowered acoustic Doppler current profilers (LADCP) (e.g. Kunze et al., 2006; Naveira Garabato et al., 2004) However, such estimates involve a number of approximations whose accuracy has not been fully determined. Fine-scale measurements also require careful processing of the raw data in order to minimize the effects of instrument noise and measurement errors (Gargett and Garner, 2008; Gille et al., 2009).

In the Southern Ocean, estimates of κ made by Sloyan (2005) from hydrographic profiles sampled by the World Ocean Circulation Experiment (WOCE) showed enhanced mixing over regions of rough bathymetry, extending to depths of at least 1500 m. LADCP and expendable CTD (XCTD) measurements in Drake Passage also showed high diffusivity values (Naveira Garabato et al., 2004; Thompson et al., 2007), with distinctly different regimes north and south of the Polar Front (Thompson et al., 2007). Mixing due to internal tides has been shown to to affect the natural iron fertilization of phytoplankton blooms (Blain et al., 2007). Yet the full extent of mixing variability in the Southern Ocean is still poorly understood, due to the limited availability of observations.

In this chapter, we consider two commonly-used methods of computing fine-scale estimates of diapycnal diffusivities. We compute our estimates from CTD and XCTD data collected in a low-mixing region in the southeastern Pacific sector of the Southern Ocean, as well in Drake Passage, where previous studies have observed enhanced mixing over rough topography (Naveira Garabato et al., 2004; Heywood et al., 2002; Thompson et al., 2007). We compare the CTD and XCTD estimates, and calibrate both against the more accurate estimates produced by microstructure measurements and and tracer diffusion. The goal of this analysis is twofold. First, we wish to assess the

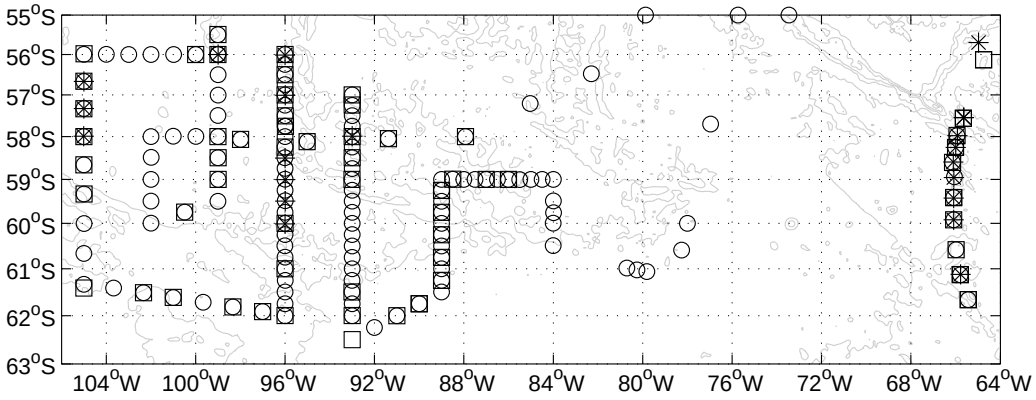

Figure 3.1: Locations of CTD stations (circles), XCTD stations (stars), and microstructure profiler stations (squares) sampled during the summer 2010 DIMES survey.

effects of instrument choice, data filtering and pre-processing methods, and estimation methods on the magnitude of κ estimates in different mixing regimes. Second, we wish to consider whether fine-scale measurements, which cannot resolve the smallest density overturns that characterize the mixing in the Southern Ocean, can still produce accurate estimates of diffusivity by resolving the larger overturns.

3.2 Data

Fine-scale and microstructure data were collected during January and February 2010 by the *R/V Thomas G. Thompson* as part of the Diapycnal and Isopycnal Mixing Experiment in the Southern Ocean (DIMES). The survey area covered a region between the PF and the SACCF in the southeastern Pacific, as well as a transect across Drake Passage near 65°W. A total of 140 CTD profiles, using two sets of Seabird SBE 9*plus* sensors, and 25 XCTD profiles were sampled, as well as 65 microstructure profiles at locations shown in Figure 3.1. All three instruments were deployed concurrently where possible, providing an opportunity to calibrate fine-structure mixing estimates against microstructure measurements. Four of the CTD casts were deployed to target depth of 5000 m, and the rest were deployed to 2000 m or to 10 m above the bottom. However, XCTDs sample to a maximum depth of 1100 m. To facilitate comparison between the two instruments, only data from the top 1000 m were used for our analysis.

Microstructure measurements were sampled with the High Resolution Profiler 2 (HRP2) provided by Woods Hole Oceanographic Institution, and the Deep Microstructure Profiler (DMP), provided by Rockland Scientific International, Inc.. A total of 43 sections were sampled with HRP2, and 22 sections with the DMP 2. Ledwell et al. (2011) provide detailed information about the instruments and the sampling methodology. The temperature profiles were averaged into 0.5 m bins for the HRP2 and into 1 m bins for the DMP. To maintain greater consistency in the comparison between our microstructure and fine-scale estimates, only the HRP2 profiles were used in our analysis.

3.3 Methods

3.3.1 Data pre-processing and overturn validation

The accuracy of Thorpe scale calculations depends on our ability to distinguish real density overturns from measurement error caused by factors such as instrument

noise, salinity spiking, and ship effects. We used a combination of several methods to minimize measurement errors in the raw data before testing for overturns.

XCTDs sample at approximately 14 cm vertical resolution. They fall freely through the water column, and are not affected by ship motion. However, they are still subject to instrument noise and to salinity spiking caused by the lag in the time responses between the temperature and conductivity sensors. Gille et al. (2009) examined the profiles and spectra from over 300 XCTD casts and found that almost all XCTDs exhibit anomalous spectral spikes at the 5 and 10 Hz frequencies in both the temperature and the conductivity spectra. To remove the spectral energy at these frequencies, they developed a method for designing a low-pass filter to remove all energy at frequencies of 5 Hz or greater. Applying the same method to our data, we designed a 21-pt filter where the spectral energy tapers from 1 to 0 in the frequency range between 22% and 34% of the Nyquist frequency. The filtered and unfiltered spectra for the DIMES profiles sampled in Drake Passage are shown in Figure 3.2. The filtered XCTD profiles have an effective vertical resolution of approximately 2 m.

To estimate the remaining noise in our filtered data, we followed the procedure described in Gargett and Garner (2008) and examined individual density profiles, defining the noise level for each profile to be the standard deviation of detrended density values within a 10 m layer where density is well-mixed. Based on this criterion, the noise level for our XCTD data was determined to be approximately 0.001 kg m^{-3}, and the noise level for CTD data was approximately 0.0004 kg m^{-3}. At depths between 600 and 1000 m for typical low-stratification profiles in our study region, density changes of 0.001 kg m^{-3} occur over depth changes of 3-4 m, and changes of 0.0004 kg m^{-3} occur over 0.5-1.5 m. To reduce the number of false overturns, we discarded all XCTD overturns of less than 4 m and all CTD overturns of less than 1.5 m, or having a density difference of less than twice the instrument noise.

Galbraith and Kelley (1996) have proposed an additional water mass test designed to reduce the number of false overturns caused by the mismatch in sensor response times, particularly in regions where temperature and conductivity vary rapidly

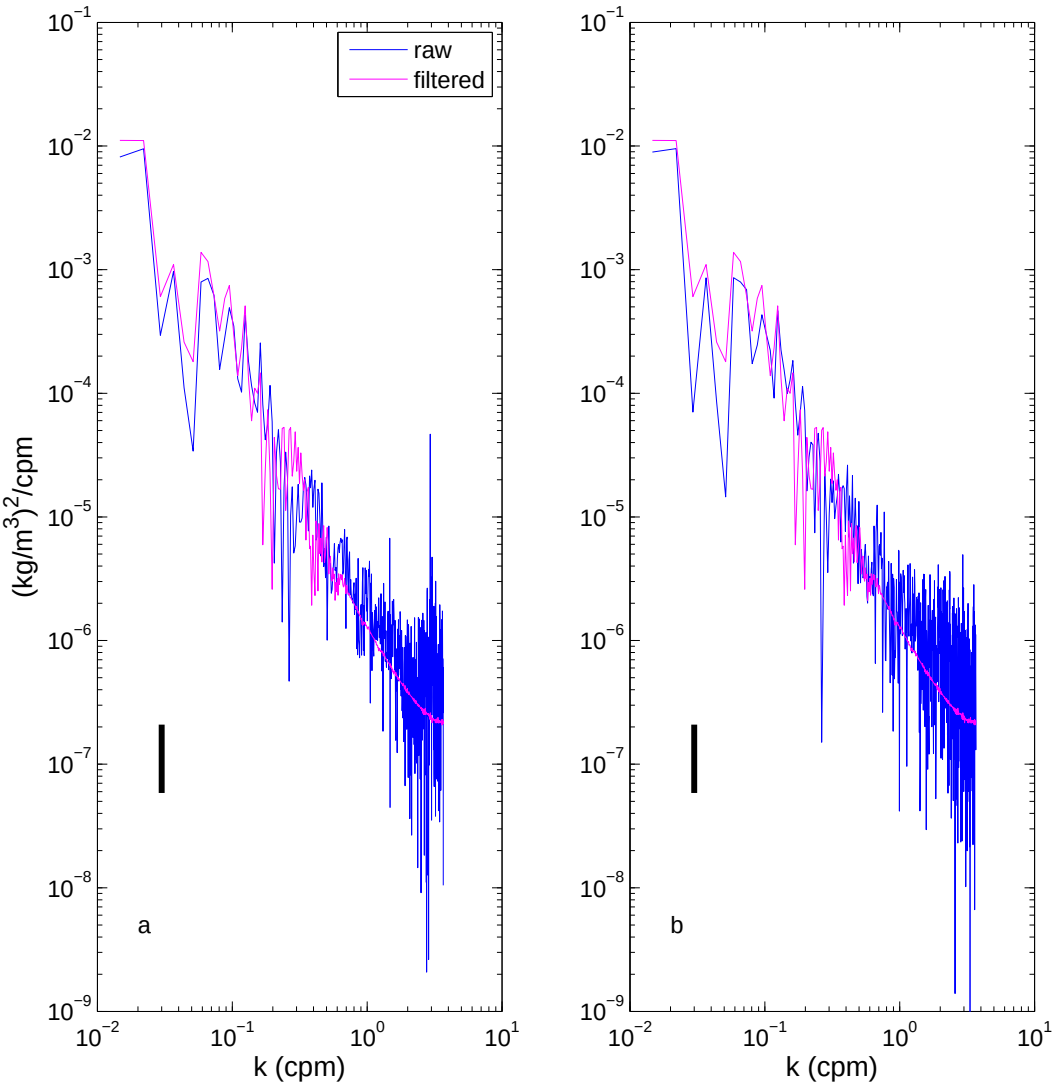

Figure 3.2: Comparison of raw and filtered spectra of (a) temperature and (b) conductivity for XCTD profiles sampled in Drake Passage during the 2010 DIMES survey. Spectra from 10 casts were calculated from detrended 1000-pt profile segments centered on 600-m depth, then averaged together.

with depth. The test is based on performing least-square fits to temperature and salinity within each overturn and computing the RMS of the differences between the fitted lines and the data. The results are then normalized the RMS difference between the sorted and the unsorted density values within the same overturn to produce the quantities ζ_t for temperature and ζ_s for salinity. The quantity ζ=max(ζ_s, ζ_t) can then be used as a measure of the tightness of the T-S relationship within the overturn. Galbraith and Kelley (1996) proposed ζ <0.5 as the threshold for overturn validation. However, Martin and Rudnick (2007) and Thompson et al. (2007) have found that a less stringent criterion of ζ <1 is sufficient, and our visual inspection of the T-S profiles confirmed this observation.

The temperature and conductivity sensors on the 9*plus* CTD sample at 24 Hz. At typical winch speeds, this results in a vertical spatial resolution of approximately 3 cm. However the resolution will vary with changes in winch speed. CTDs are also subject to ship roll, and show differences in response times for temperature and conductivity sensors (referred to as "thermal lag"), which can result in salinity spiking. Sea-Bird Electronics provides software routines for reducing thermal lag. We performed the suggested correction using values of thermal anomaly amplitude α=0.03 and thermal anomaly time constant τ=7, as recommended in the Sea-Bird manual (Sea-Bird Electronics, Inc.). The settings for the filter used for salinity spiking reduction were determined by an iterative procedure determined by Gargett (2008, personal communication) following Morrison et al. (1994). Pressure reversals caused by ship roll were removed from the profiles, and the processed data were binned into 25 cm depth bins. As a final step in reducing noise-related false overturns, we followed Gargett and Garner's (2008) method of creating an intermediate density profile in which a constant density is maintained until a density change greater than a specified threshold value occurs between two successive data points. A sample section of such a profile overlaid over the original data is shown in Figure 3.3.

Potential overturns in the intermediate CTD profiles were then evaluated based on Gargett and Garner's (2008) overturn ratio criteria, replacing the Galbraith and Kelley (1996) criteria used for XCTD data:

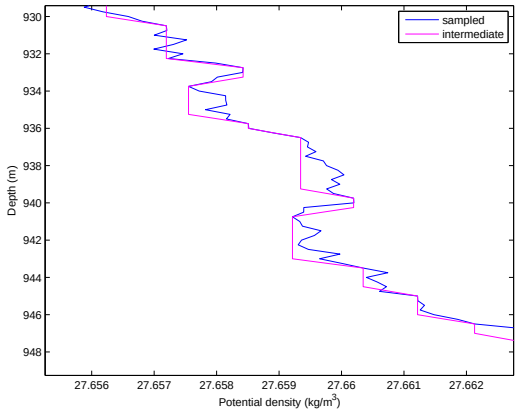

Figure 3.3: Sample segment of a Drake Passage density profile (blue) and an intermediate profile (magenta) generated following the method in citetgargett. The density threshold level for generating the intermediate profile was $2 \times \delta_D$, where δ_D=0.0004 is the instrument noise level.

$$R_0 = min(L^+/L, L^-/L), \tag{3.1}$$

where L is the length of an overturn, L^+ is the length of that portion of L where the Thorpe displacements are positive, and L^- is the length of the portion where the displacements are negative. Values of $R_0 < 0.2$ implied that the prospective overturn was caused by a single density spike that might have been due to instrument noise, and overturns with these values were rejected.

For both CTD and XCTD data, the results for each cast were averaged into 100 m depth bins, and error bars were calculated using the bootstrap method (Efron and Gong, 1983).

3.3.2 Thorpe scale analysis

Thorpe scale analysis (Thorpe, 1977) provides a method for estimating small-scale mixing rates from temperature and salinity data in places where direct microstruc-

ture measurements are not available. The goal of the analysis is to determine kinetic energy dissipation rate ϵ and diapycnal eddy diffusivity κ_ρ. The value of ϵ is related to the Ozmidov scale L_O (Ozmidov, 1965) by

$$\epsilon = L_O^2 N^3, \tag{3.2}$$

where N is the buoyancy frequency.

The Thorpe scale L_T is obtained by reordering a vertical profile that contains density overturns into a stably stratified profile. It is defined as

$$L_T \equiv \sqrt{\langle d'^2 \rangle}, \tag{3.3}$$

where Thorpe displacement d' is the displacement of every reordered point from its original position in the profile.

Comparisons between L_O and L_T suggest a linear relationship between the two scales (Dillon, 1982; Crawford, 1986). Dillon (1982) found the coefficient to be $L_O = (0.8 \pm 0.4) L_T$. Substituting this relationship into (3.2) gives

$$\epsilon_i = 0.64 L_{Ti}^2 \langle N \rangle_i^3, \tag{3.4}$$

where i refers to the ith overturn.

Diapycnal eddy diffusivity can be computed from ϵ as

$$\kappa_\rho = \Gamma \epsilon N^{-2}, \tag{3.5}$$

where Γ is the mixing efficiency. Here we follow common convention (e.g. Thompson et al. (2007)) and assume Γ=0.2.

3.3.3 Vertical strain analysis

An alternate method of estimating κ_ρ derives from examining the energy spectra of vertical strain in the internal wave field. In the stratified ocean, non-linear interactions

among internal waves transfer energy from higher wavelengths to increasingly unstable, smaller wavelengths, eventually leading to turbulence. Comparison of various wave-dissipation models (Wijesekera et al., 1993) has shown that κ_ρ estimates that are in good agreement with observational data can be obtained by comparing the spectrum of the internal-wave-field strain rates to a model GM spectrum proposed by Garrett and Munk (1975).

Strain variance level $\langle \xi_z^2 \rangle$ is computed by integrating the Fourier-transformed spectral representation ϕ_λ of the buoyancy frequency to determine the maximum wavenumber k_{max} such that

$$\langle \xi_z^2 \rangle = \int_{k_{min}}^{k_{max}} \phi_\lambda \mathrm{d}k = 0.2, \tag{3.6}$$

where the minimum wavenumber k_{min} = 0.01.

The strain variance level for the GM spectrum is computed for the same wavenumber range as

$$\langle \xi_z^2 \rangle_{GM} = \frac{\pi E_0 b j_*}{2} \int_{k_{min}}^{k_{max}} \frac{k^2}{(k + k_*)^2} \mathrm{d}k, \tag{3.7}$$

where E_0 is the dimensionless energy level, b is the scale thermocline depth, j_* is the reference mode number and $2\pi k_*$ is the reference wavenumber, defined as 0.0073(N / N_0). Following Gregg and Kunze (1991), we set these parameters to be E_0 = 6.3 $\times$ 10^{-5}, b=1300 m, j_* = 3, and N_0 = 0.00524 s^{-1}.

Strain-derived vertical diffusivity κ_ρ^ϕ can be calculated from (3.6) and (3.7) as

$$\kappa_\rho^\phi = \kappa_0 \frac{\langle \xi_z^2 \rangle^2}{\langle \xi_z^2 \rangle_{GM}^2} H(R_\omega) J(f, N), \tag{3.8}$$

with κ_0 = 0.05 $\times$ 10^{-4} m^{2}s^{-1}.

H and J are empirical functions that account for the effect of latitude on the internal wave field. The function H is given as

$$H(R_\omega) = \frac{3R_\omega(R_\omega + 1)}{4(R_{\omega GM}^2)} \sqrt{\frac{2}{R_\omega - 1}}, \tag{3.9}$$

where R_ω=$\langle V_z^2 \rangle / (N^2 \langle \xi_z^2 \rangle)$ is the shear/strain ratio, with V_z being the vertical derivative of horizontal velocity. For our calculations, we set R_ω=10 (Naveira Garabato et al., 2004; Thompson et al., 2007). J is given as

$$J(f, N) = \frac{f cosh^{-1}(N/f)}{f_{30} cosh^{-1}(N_0/f_{30})}, \tag{3.10}$$

where f_{30}=7.29 $\times$ 10^{-5}s^{-1} is the Coriolis frequency at 30° latitude.

Thompson et al. (2007) used Equation 3.8 to calculate spectra based on both buoyancy frequency and potential density profiles across Drake Passage, and found that both quantities produced spectra of similar amplitudes, with differences of less than 15%. Both spectra also showed the same spatial pattern of κ_ρ values across the passage. For our analysis, we used buoyancy frequency spectra, computed using the method described by Kunze (2003) and followed by Thompson et al. (2007).

To compare the vertical strain diffusivities for CTD and XCTD data, we computed κ_ρ^ϕ estimates for the CTD and XCTD sections sampled over two eastern Pacific transects and one Drake Passage transect during the DIMES survey, using an averaged value of the Coriolis parameter, f=-60.7°, for each transect. For every buoyancy frequency profile in the transect, we divided the data into 100-m depth bins, discarding the top 200 m to eliminate the mixed layer and the effects of ship's draft near the surface. We normalized the data in each bin by the average buoyancy frequency for that bin, then subtracted a linear trend before computing the spectrum. We then averaged the spectra over all casts in each bin. The resulting spectra for the XCTD and CTD, as well as the GM spectrum, are shown in Figure 3.4 for the mid-depth bins for all the stations in the Drake Passage transect. The error bars on the spectra represent the 95% confidence interval, computed based on the χ^2 cumulative distribution of the spectra (Bendat and Piersol, 2000).

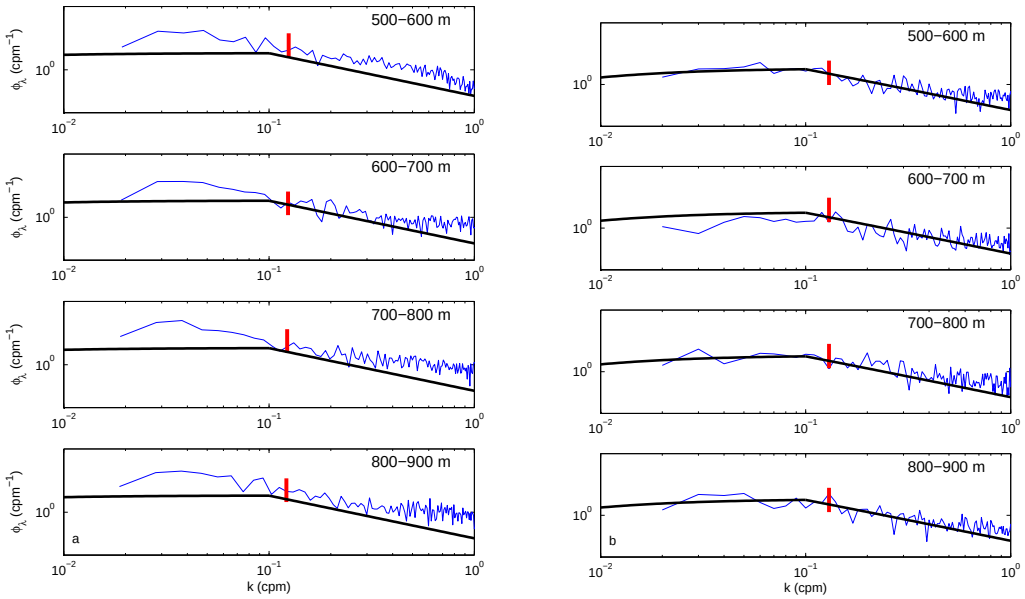

Figure 3.4: Comparison between vertical spectra of buoyancy frequency (blue) for the (a) XCTD and (b) CTD stations in Drake Passage, and the GM model spectrum (thick black line). Vertical red lines indicate the spectral uncertainty.

3.4 Results and discussion

3.4.1 CTD vs. XCTD

Thorpe scale method

The diffusivity estimates produced by both Thorpe scale and vertical strain methods are affected by the properties of the instruments used to obtain the density profiles. To examine the effect of instrument choice on our κ estimates, and to assess the potential accuracy of such estimates in the low-stratification regime of our sampling region, we compare values of κ obtained from three DIMES transects in which CTDs and XCTDs were deployed concurrently. Two of the transects were located in the eastern Pacific sector of the Southern Ocean, near 105°W and 96°W. The third transect was sampled in Drake Passage, near 65°W. The station locations for the transects are shown in Figure 3.1.

Thorpe scale CTD and XCTD estimates of κ in the upper 1000 m for all three transects are shown in Figure 3.5. Previous fine-scale observations in Drake Passage have indicated that the mixing in that region is enhanced by the flow of the ACC over rough topography, with reported values of κ ranging from $O(10^{-4})$ to $O(10^{-2})$ m^2 s^{-1} (Thompson et al., 2007; Naveira Garabato et al., 2004) . These results are consistent with DIMES microstructure and tracer diffusion estimates, which estimated values of κ ranging from 1×10^{-4} to 3×10^{-4} m^2 s^{-1} (L. St. Laurent, 2011, personal communication). Both sets of estimates in Figure 3.5 show values of a similar order of magnitude. The magnitude and vertical structure of the CTD estimates is consistent with the estimates made by Sloyan et al. (2010) in the southeastern Pacific during austral winter of 2005 and austral summer of 2006, with κ values being highest below the mixed layer and decaying with depth. However, neither the CTD nor the XCTD estimates show statistically significant differences between the eastern Pacific transects and the Drake Passage transects, even though the results from tracer diffusion and from microstructure measurements suggest that values of κ in the eastern Pacific are only on the order

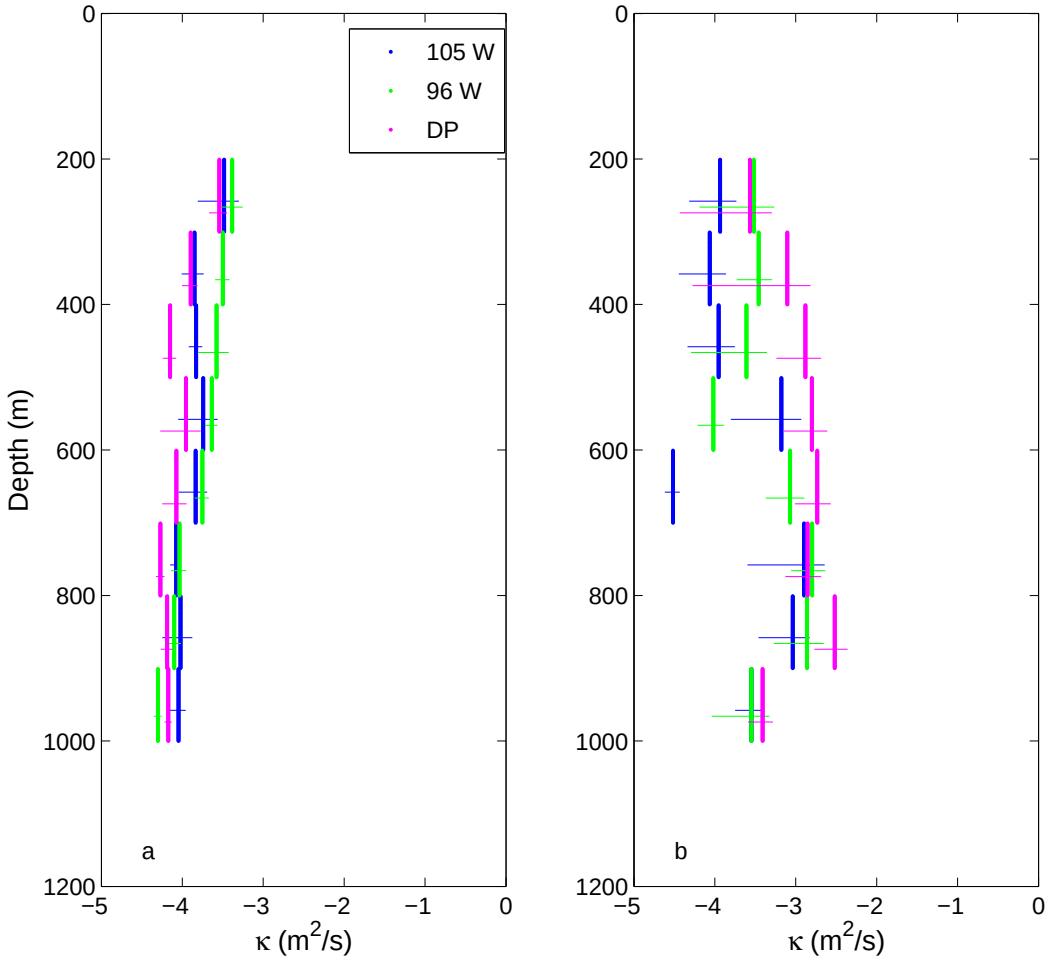

Figure 3.5: Thorpe scale estimates of κ computed from (a) CTD and (b) XCTD data sampled during the DIMES survey in January and February 2010.

of 10^{-5} m^2 s^{-1} (Ledwell et al., 2011). The XCTD estimates show a wider range for κ, with values for the 105°W and 96°W transects roughly an order of magnitude lower than the Drake Passage values in the 300-700 m depth range. However, the larger error bars for the XCTD estimates suggest that the difference may be due to instrument noise. In addition, equations 3.5 and 3.4 indicate that, based on the typical buoyancy frequencies of N^2=$O(10^{-5})$ observed in our survey region, Thorpe scales needed to produce κ values on the order of 10^{-5} m^2 s^{-1} are approximately 10 cm. Such small overturns cannot be resolved by either the CTD or the XCTD data, given the noise thresholds estimated in Section 3.3.1. By detecting only the largest overturns in the density profiles, both instruments will tend to overestimate the mixing.

Vertical strain method

Estimates of κ computed using the vertical strain analysis described in Section 3.3.3 are shown in Figure 3.6. The order of magnitude of the estimates for both the CTD and the XCTD is consistent with the Thorpe scale estimates in Figure 3.5, and the XCTD estimates once again show a wider range of values and larger error bars than the CTD estimates. The CTD estimates show what appears to be a statistically significant difference between Drake Passage and the eastern Pacific transects below 700 m, corresponding to the depth range where Drake Passage stratification is lowest compared to the other transects (Figure 3.7). Low-stratification regimes can lead to enhanced mixing, due to greater instability allowed by small density changes. However, they are also susceptible to overestimation due to small measurement errors. It is uncertain how much of the spatial structure in our estimates is due to instrument noise.

In addition to having greater variability, XCTD estimates produce higher values of κ than the CTD estimates, with Drake Passage values an order of magnitude larger below 400 m, and eastern Pacific values becoming larger below 600 m. A comparison of CTD and XCTD density spectra (Figure 3.8) shows increased levels of white noise at higher wavelengths in the XCTD spectrum as compared to the CTD, despite the ap-

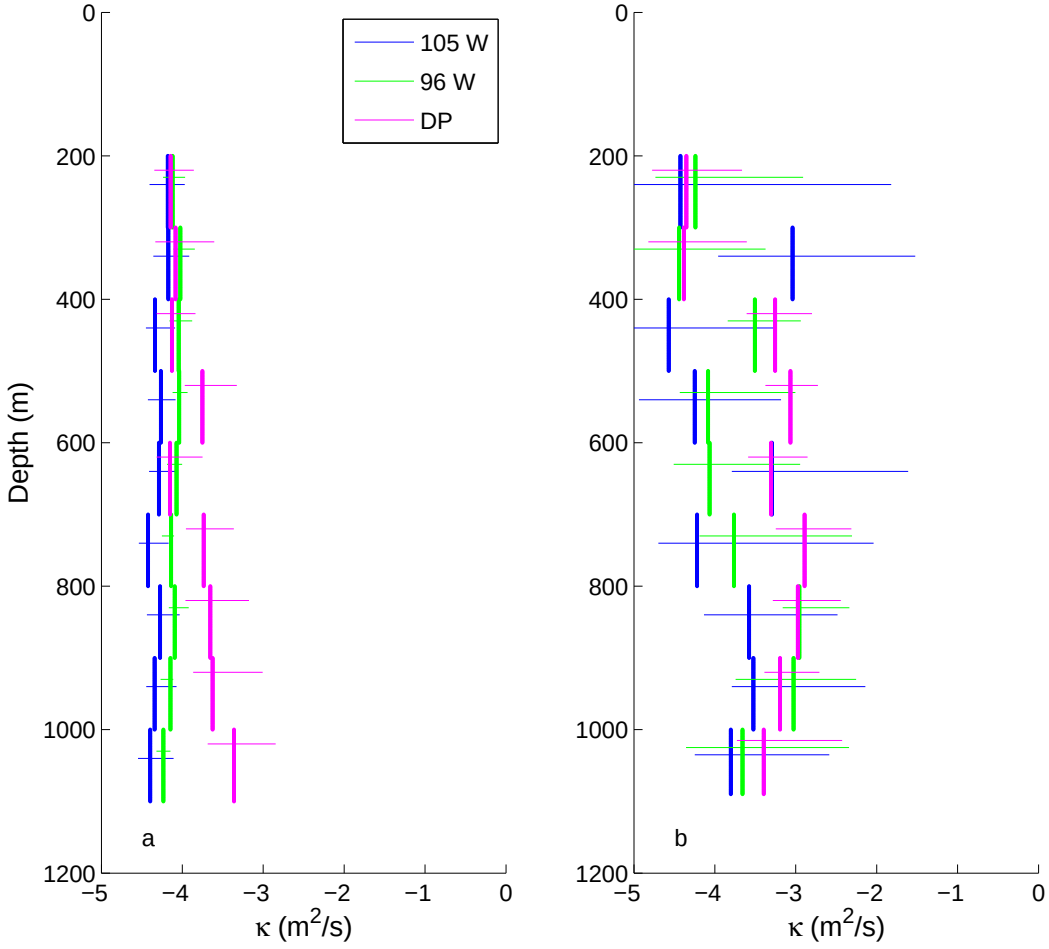

Figure 3.6: Vertical strain estimates of κ computed from (a)CTD and (b)XCTD data sampled during by the DIMES survey during January and February 2010. The colors are as in Figure 3.5.

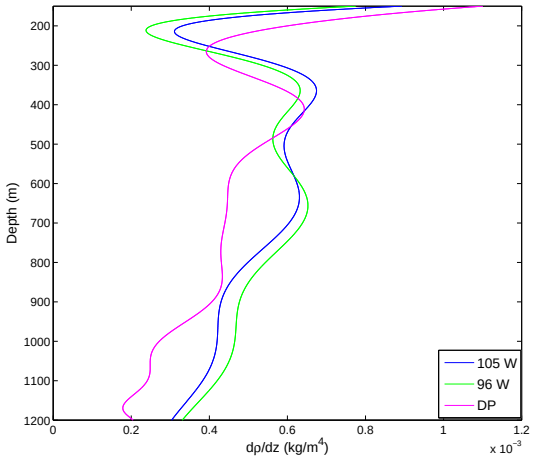

Figure 3.7: Stratification ($d\rho/dz$) in Drake Passage, at 96°W and at 105°W, based on CTD profiles sampled during the 2010 DIMES survey.

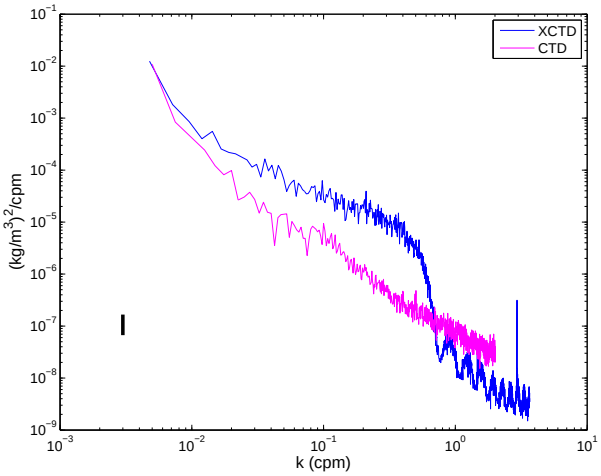

Figure 3.8: Comparison of mean CTD and XCTD spectra in the 400-800 m depth range, using averaged spectra from 19 stations where both instruments were sampled. Black vertical bar represents the spectral error.

plication of the 21-point filter described in Section 3.3.1. The difference between the two spectra suggests that the filtered XCTD data still retain significant instrument noise. Filtering at lower wavenumbers would reduce the noise, but at the cost of increasing the minimum resolvable overturn size to approximately 10 m, further reducing the accuracy of the resulting estimates.

3.4.2 Comparison with microstructure

Figure 3.9 shows Thorpe scale estimates from the DIMES CTD data and from microstructure measurements sampled with the HRP2 profiler during the same survey. Due to issues with salinity spiking, only the temperature profile for the HRP2 was available, therefore the Thorpe scales for both the CTD and CTD data were determined from temperature overturns. The HRP2 data were binned into 50 cm depth bins, and the same validation criteria, as described in Section 3.3.1, were used for both instruments. The transects shown in the figure were sampled at 96°W, 93°W, and in Drake Passage at 65°W.

The diapycnal diffusivities computed from the centimeter-scale velocity shear measured by the HRP2 indicate that, in the southeastern Pacific sector of our sampling region, κ=(0.75 $\pm$ 0.07)$\times$ 10^{-5} m^2 s^{-1} (Ledwell et al., 2011). In Drake Passage, the estimates rise to $O(10^{-4}$ m^2 s^{-1} (L. St. Laurent, 2011, personal communication). However, the Thorpe scale estimates shown in Figure 3.9 produce κ values that are 1 to 3 orders of magnitude larger. At depths below 500 m, where most of the overturns were found, the CTD and the HRP2 produce κ ranging from 10^{-3} to 10^{-1} m^2 s^{-1}, values that exceed both the microstructure measurements and the density-based estimates from CTD and XCTD. The HRP2 Thorpe estimates for Drake Passage were lower than the estimates for the 96°W and 93°W transects, in contradiction with previous findings (Heywood et al., 2002; Naveira Garabato et al., 2004). These results suggest that in the typical stratification regimes of the Southern Ocean, temperature-based estimates in the top 1000 m are dominated by salinity-compensated overturns that produce no turbulence, and will

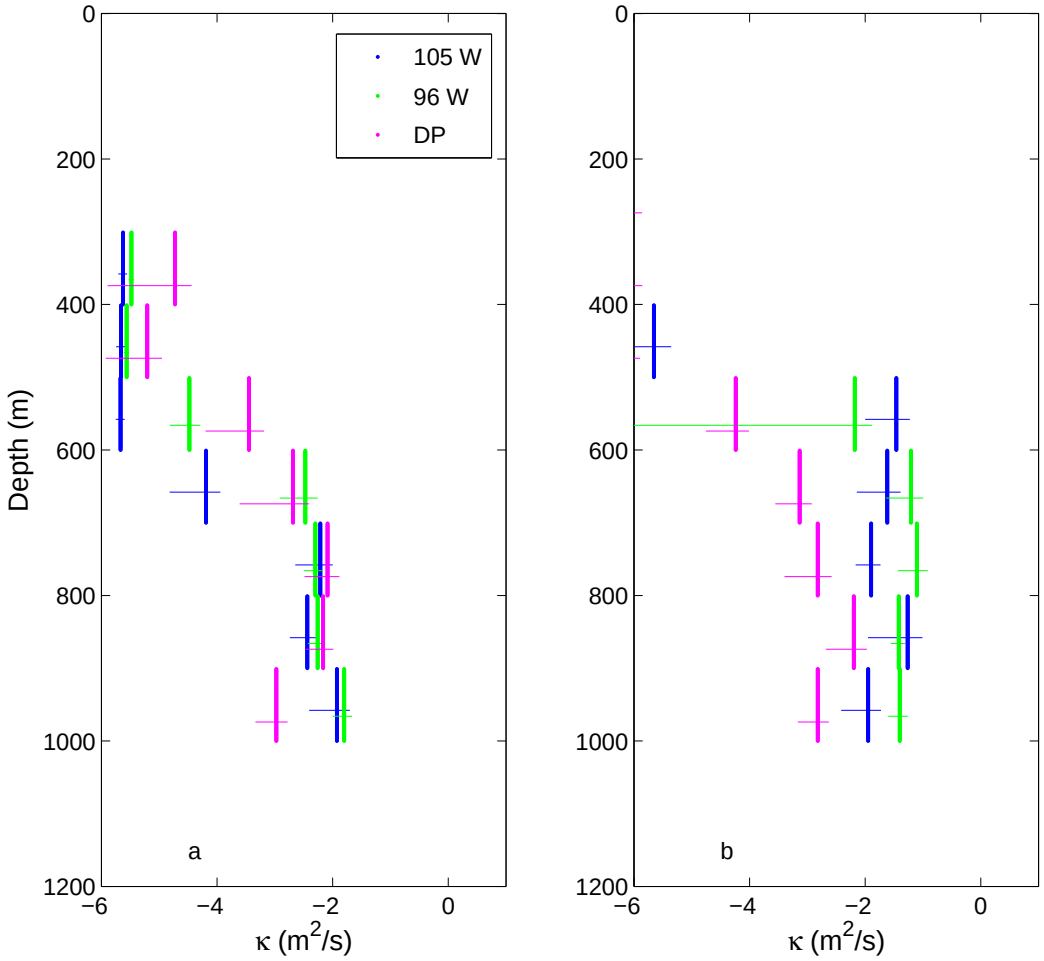

Figure 3.9: Temperature-based Thorpe scale estimates of κ computed from (a) CTD and (b) HRP2 data sampled during by the DIMES survey during January and February 2010.

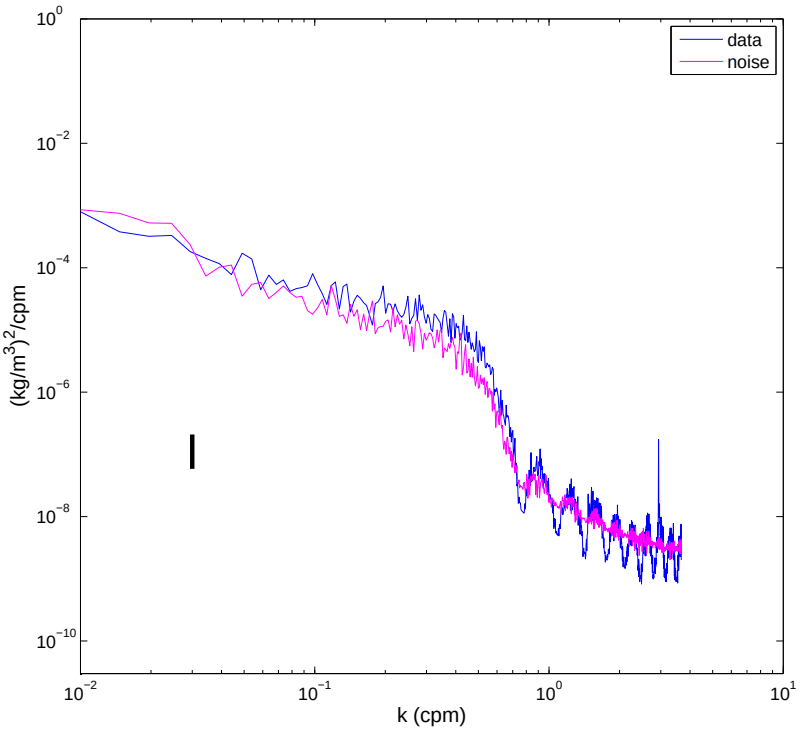

Figure 3.10: Averaged density spectrum (blue) in the 200-400 m depth range, computed from 10 XCTD profiles sampled in Drake Passage, and the corresponding synthetic spectrum (magenta) generated by superimposing red noise over the background stratification. Black vertical bar represents the spectral uncertainty.

therefore overestimate the diffusivity even compared to the already high density-based estimates.

3.4.3 Comparison with synthetic data

The results from the previous section raise the possibility that in a low stratification regime characterized by small density overturns, κ estimates from CTD and XCTD data may be dominated by instrument noise. To further evaluate the effects of noise, we repeated the Thorpe scale calculations using synthetic data generated by adding red

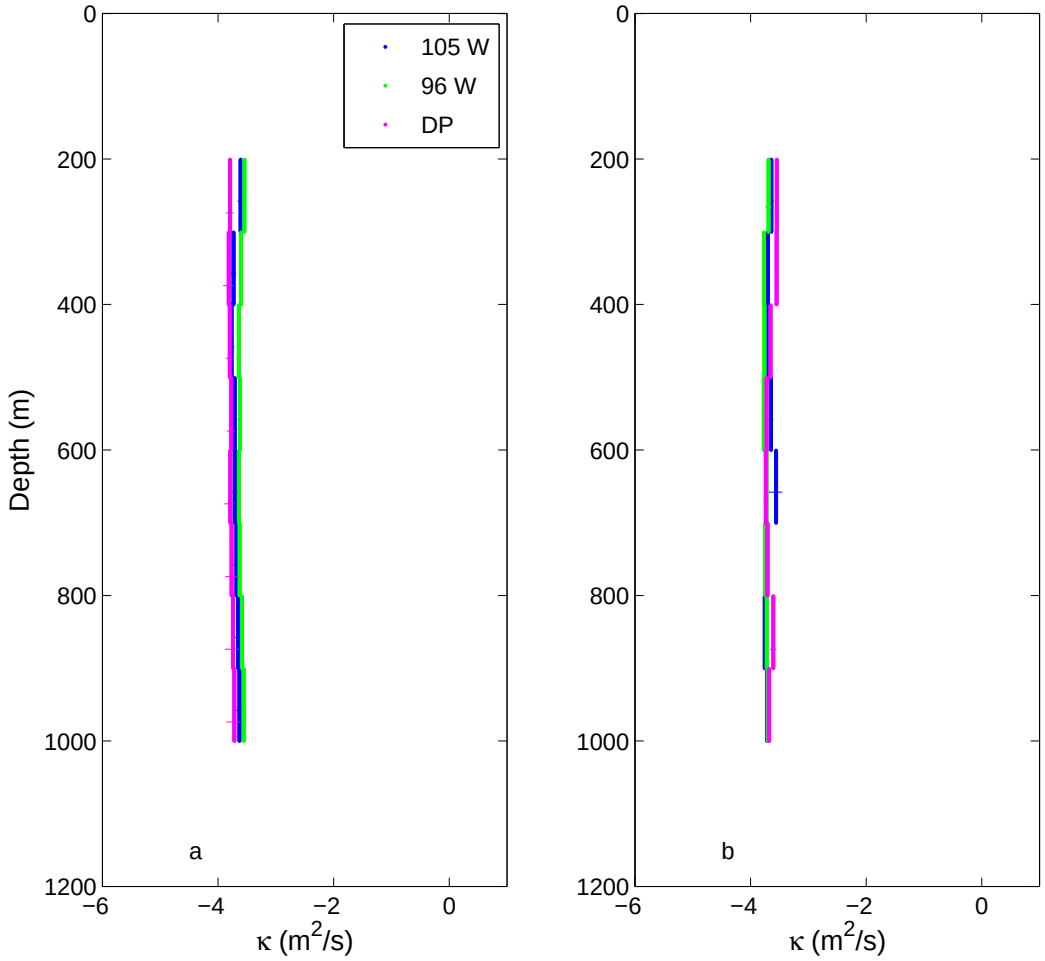

Figure 3.11: Thorpe scale estimates of κ computed from synthetic red noise superimposed on background stratification for (a)CTD and (b)XCTD data.

noise to the background stratification of our observed data. For every CTD and XCTD cast, we created a background profile by fitting a straight line to every 100 m segment of the original density profile. We then generated a vector of red noise by filtering white noise to match the standard deviation and spectral slope of the data, and added the noise to the background profile to create our synthetic data set. A comparison observed and corresponding synthetic spectra is illustrated in Figure 3.10.

A set of 50 synthetic profiles was generated for every observed profile, and κ estimates were computed for 100 m depth bins using the Thorpe scale method. The resulting κ profiles, based on the background stratifications observed for the 105°W, 96°W and Drake Passage transects, are shown in Figure 3.11. For both the CTD and the XCTD, all estimates converge to κ=10^{-4} m^2 s^{-1}, regardless of depth or of the small differences in background stratification between the Drake Passage and eastern Pacific profiles. Therefore, the diffusivity estimates calculated from our CTD and XCTD data cannot be readily distinguished from estimates produced entirely by instrument noise.

3.5 Summary

Fine-scale estimates of diapycnal diffusivities in the Southern Ocean were computed from CTD and XCTD data sampled during the DIMES survey in January and February of 2010. Both the Thorpe scale and the vertical strain method produced values of κ on the order of 10^{-4} m^2 s^{-1}. While such estimates appear consistent with microstructure measurements sampled in Drake Passage during the same cruise, they do not reproduce the differences in diffusivity that have been measured between Drake Passage and the low-mixing region in the eastern Pacific section of the survey. A close examination of the noise characteristics of both instruments indicates that once the data have been processed to minimize instrument noise, salinity spiking and ship effects, the minimum size of resolvable density overturns is approximately 1.5 m for CTD data and 4 m for the XCTD. Such a resolution is insufficient to resolve the small overturns that generate most of the mixing in the survey region. Synthetic profiles generated by su-

perimposing red noise over background stratification curves fitted to the data produced estimates of κ with the same order of magnitude as the estimates computed from the data itself.

The relatively low cost and wide availability of XCTD and CTD data compared to microstructure data have led to widespread use of fine-scale methods for estimating mixing in the global ocean. Our analysis leads us to conclude that CTD and XCTD measurements cannot reliably resolve the small-scale mixing in the low-stratification regime characteristic at mid-water depths of the Southern Ocean. However, both the Thorpe scale and the strain method have the potential to produce accurate estimates in regions where the stratification is high and mixing is characterized by large density overturns. A thorough examination of each individual instrument's noise properties, and a careful selection of an appropriate data filter are required when fine-scale methods are employed.

Chapter 4

Horizontal and vertical processes contributing to natural iron supply in the mixed layer

4.1 Introduction

The waters of the Shackleton Fracture Zone (SFZ) in southern Drake Passage (Figure 2.1a) display an uneven distribution of surface Chlorophyll-a (Chl-a) in the vicinity of the Shackleton Transverse Ridge (STR). Satellite imagery of the region (Figure 2.1b) shows high Chl-a levels in the shallow waters on the continental shelf, where iron can be entrained from the sediments (Hopkinson et al., 2007). In deeper waters north of the shelf, a sharp Chl-a gradient occurs, with low Chl-a levels found to the west of the Shackleton Transverse Ridge (STR) and high Chl-a levels to the east, beginning in the Ona Basin and continuing downstream into the southern Scotia Sea (Holm-Hansen et al., 2004; Kahru et al., 2007).

Biological productivity in the Southern Ocean has been shown to be iron-limited (Boyd, 2002; Chisholm and Morel, 1991; de Baar et al., 1995; Helbling et al., 1991; Martin et al., 1990), with persistent blooms observed in naturally iron-enriched areas

such as the Crozet Island (Planquette et al., 2006; Venables et al., 2007) and the Kerguelen Plateau (Blain et al., 2001). Shipboard iron incubations indicate that that phytoplankton biomass in the Ona Basin is also iron-limited away from the continental shelf (Helbling et al., 1991; Hopkinson et al., 2007). Observations in high-Chl-a regions suggest that iron is supplied to waters away from the shelf via horizontal advection and eddy-driven processes such us eddy pumping, cross-frontal mixing, and the formation of small-scale filaments formed by eddy interactions (Abraham et al., 2000; Kahru et al., 2007; Lapeyre and Klein, 2006; Maraldi et al., 2009; Venables et al., 2007). In a study of 10 years' worth of satellite data from the region near the Ona Basin, Kahru et al. (2007) found consistently high correlations between cyclonic eddy activity and Chl-a anomalies in the Weddell-Scotia Confluence during September and October. Their findings suggest that eddy-driven upwelling and cross-frontal northward iron transport could account for a significant part of the variability of the spring bloom. However, the higher Chl-a levels in the region persist throughout the summer, and Kahru et al. (2007) found no clear correlation between eddy activity and bloom intensity from January through March. In this chapter, we consider the vertical iron fluxes driven by diapycnal mixing and mixed-layer entrainment, and examine the hypothesis that these fluxes can provide the additional iron needed to sustain the late summer bloom in our study region.

Hydrographic studies in the vicinity of the STR and the South Shetland Islands have found evidence that iron is entrained from the sediments in the shallow waters on the continental shelf, and distributed off-shore by horizontal advection. (Hopkinson et al., 2007; Zhou et al., 2010a) In this chapter, we use a 13-year time series of satellite data to examine the relationship between Chl-a levels in the Ona Basin and off-shore advection driven by frontal movement. We then consider a combination of *in situ* data and mixed-layer climatologies to estimate the effects of small-scale diapycnal mixing and mixed-layer entrainment, which may provide a vertical supply of additional iron into the mixed layer to sustain the Chl-a concentrations in months when horizontal advection alone is not sufficient. Finally, we use a one-dimensional numerical model to to examine the combined effects of mixing and entrainment on the iron supply in the top 30 m in

the Ona Basin during the months of January through April.

4.2 Data and methods

To evaluate the upper ocean circulation in our study region, we obtained weekly maps of gridded sea level anomalies (SLA) for the months of November through April from 1997 to 2010 from AVISO (Archiving, Validation and Interpretation of Satellite Oceanographic Data) (Ducet et al., 2000). AVISO provides SLA maps gridded on a 1/3°× 1/3°Mercator grid, computed from merged satellite data. Monthly average SLAs were computed from the weekly data sets. To obtain absolute sea surface height (SSH), a mean dynamic height field computed relative to 1500 db from the World Ocean Circulation Experiment (WOCE) hydrographic climatology (Gouretski and Koltermann, 2004) was added to the anomalies.

The Antarctic Circumpolar Current (ACC) is commonly characterized as consisting of three primary fronts: the Subantarctic Front (SAF), the Polar Front (PF) and the Southern ACC Front (SACCF). However, high-resolution satellite data (Hughes and Ash, 2001) and drifter data (Niiler et al., 1991) have shown a more complicated structure consisting of multiple jets and filaments. A hydrographic study by Sokolov and Rintoul (2007a) described each of the three main fronts as having distinct multiple branches, and a follow-up study (Sokolov and Rintoul, 2009) identified each frontal branch with a specific SSH contour. Our choice of the WOCE climatology to calculate SSH values allowed us to follow the Sokolov and Rintoul (2009) definitions to identify front locations. The southern branch of the PF and both branches of the SACCF run across our study region as shown in Figure 4.1. West of the STR, the SACCF closely follows the 2000 m bathymetry contour until it reaches 58°W, where it splits into two branches. The northern branch (SACCF-n) moves northward, allowing the shelf waters east of the STR to propagate into the deeper waters of the Ona Basin.

Composite images of monthly Chl-a data were created by Mati Kahru of Scripps Institution of Oceanography from full-resolution MODIS-Aqua and SeaWiFS data down-

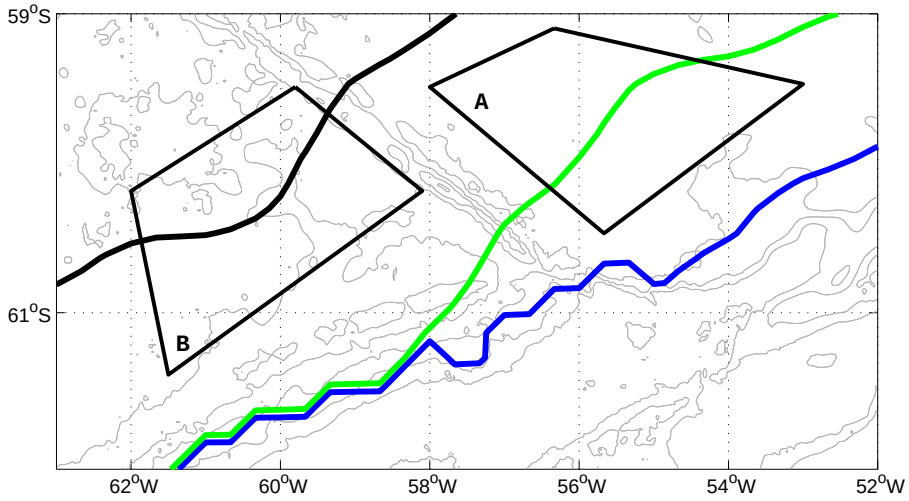

Figure 4.1: Locations of the Polar Front (black line), the northern branch of the SACCF (green line) and the southern branch of the SACCF (blue line) in southern Drake Passage, as defined by the sea surface height criteria of Sokolov and Rintoul (2009).

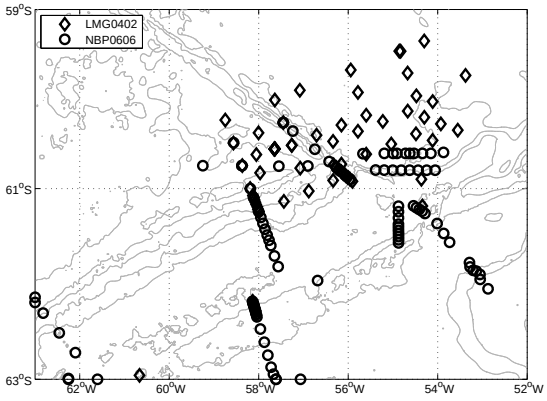

Figure 4.2: CTD station locations for the LMG0402 and NBP0606 cruises.

loaded from the Goddard DAAC. Chl-a concentrations were estimated using the standard OC4v2 chlorophyll algorithm (O'Reilly et al., 1998), which has been shown to correlate well with *in situ* measurements in the region (Holm-Hansen et al., 2004). The Chl-a values were then regridded from a 1-km grid to match the SLA grid, using a median filter with a radius of 18.5 km.

CTD data were collected in February and March 2004 by the *R/V Laurence M. Gould* (LMG0402) and in July and August 2006 by the *R/V Nathaniel B. Palmer* (NBP0606) at locations shown in Figure 4.2a, with water samples for trace metal analysis collected at selected stations. We have provided a detailed description of the sampling and methods in Section 2.2.1. Dissolved iron concentrations were originally determined within a few hours of sampling, using the flow injection analysis method (Measures et al., 1995). The samples for LMG0402 were later reprocessed using inductively coupled plasma mass spectrometry (ICP-MS) (C. Measures, 2011, personal communication). The samples for NBP0606 are expected to be reprocessed by summer of 2011.

Estimates of precipitation rates, wind velocities, and surface heat fluxes are available from the National Centers for Environmental Prediction/National Center for Atmospheric Research (NCEP/NCAR) reanalysis project (Kalnay and coauthors, 1996). The

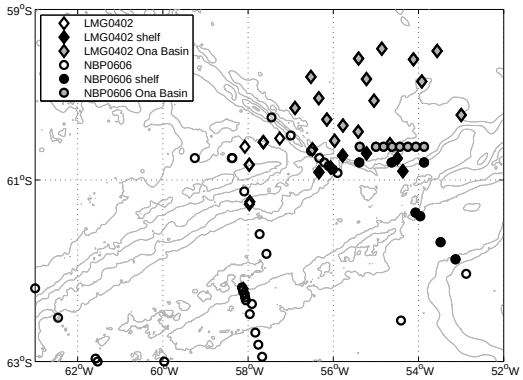

Figure 4.3: Locations of iron stations sampled during LMG0402 (diamonds) and NBP0606 (circles). Gray symbols indicate the Ona Basin stations whose profiles are plotted in Figure 4.4. Black symbols indicate the shelf stations plotted in Figure 4.6.

data are gridded by NCEP/NCAR as described by Kalnay and coauthors (1996) and are available 4 times daily. Wind stress τ was computed as τ=ρ_a C$|u|u$, where u is the wind velocity at 10 m above the sea surface, ρ_a=1.2 kg/m^2 is the density of air, and C is the drag coefficient. The values for C were taken from Yelland and Taylor (1996) for $|u| \geq$6 m/s and from Yelland et al. (1998) for$|u| <$6 m/s.

4.3 Iron distribution

Figure 4.3 shows the location of the iron stations sampled in the Ona Basin during LMG0402 and NBP0606 . The individual profiles for these stations are shown in Figure 4.4. While the LMG0402 concentrations throughout the water column are significantly lower than the NBP0606 values due to increased biological uptake of iron during the summer, both sets of profiles show the highest iron concentrations occurring below the mixed layer, in the depth range from 100 to 200 m. For the Ona Basin profiles, the iron maximum for most stations is located at a potential density surface in the range 27.5$\leq \sigma_\theta \leq$27.6. Both summer and winter data indicate the presence of high iron

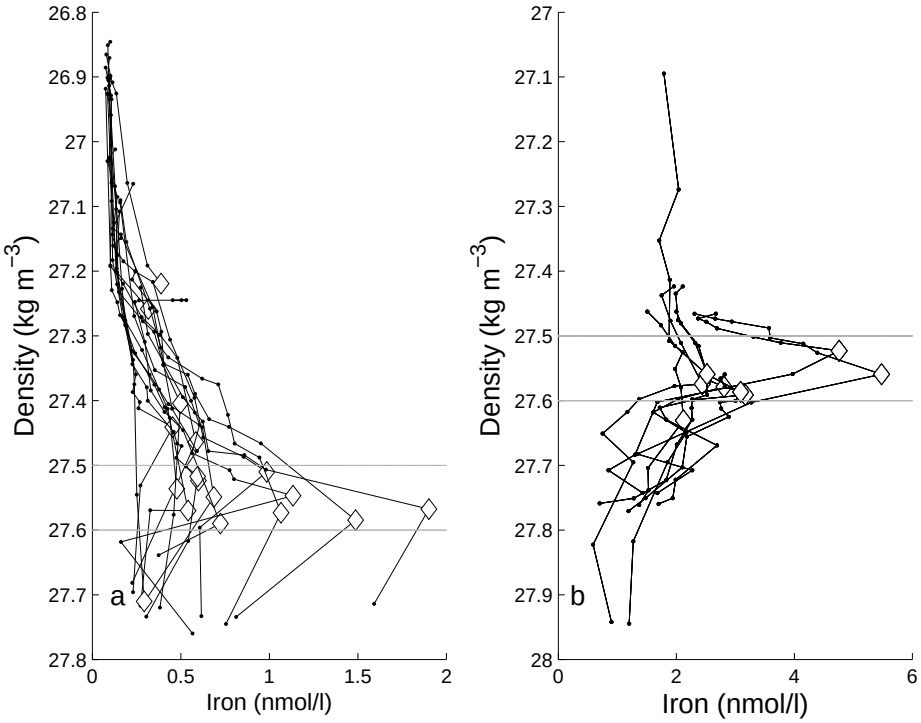

Figure 4.4: Profiles of iron concentration vs. density in the Ona Basin for (a) March 2004 (LMG0402) and (b) August 2006 (NBP0606). The 27.5$\leq \sigma_\theta \leq$27.6 density layer is indicated by the gray horizontal lines. Diamonds indicate the iron maximum at each individual station.

gradients in the top 100 m, which can also be seen in the averaged Ona Basin profiles in Figure 4.5. The presence of these gradients differentiates the Ona Basin from other high-iron regions in the Southern Ocean such as the Kerguelen Plateau (Blain et al., 2007) and allows for high upward fluxes of iron toward the base of the mixed layer.

The mean depth of the 27.5$\leq \sigma_\theta \leq$27.6 density layer in our study region is shallowest in the iron-rich shelf waters near King George Island and Elephant Island, and deepest for the low-iron ACC stations furthest off the shelf west of the STR (Figure 2.4). Ardelan et al. (2010) found high iron concentrations in the same density range in shelf waters during the summer 2006 AMLR survey. The density distribution is consistent

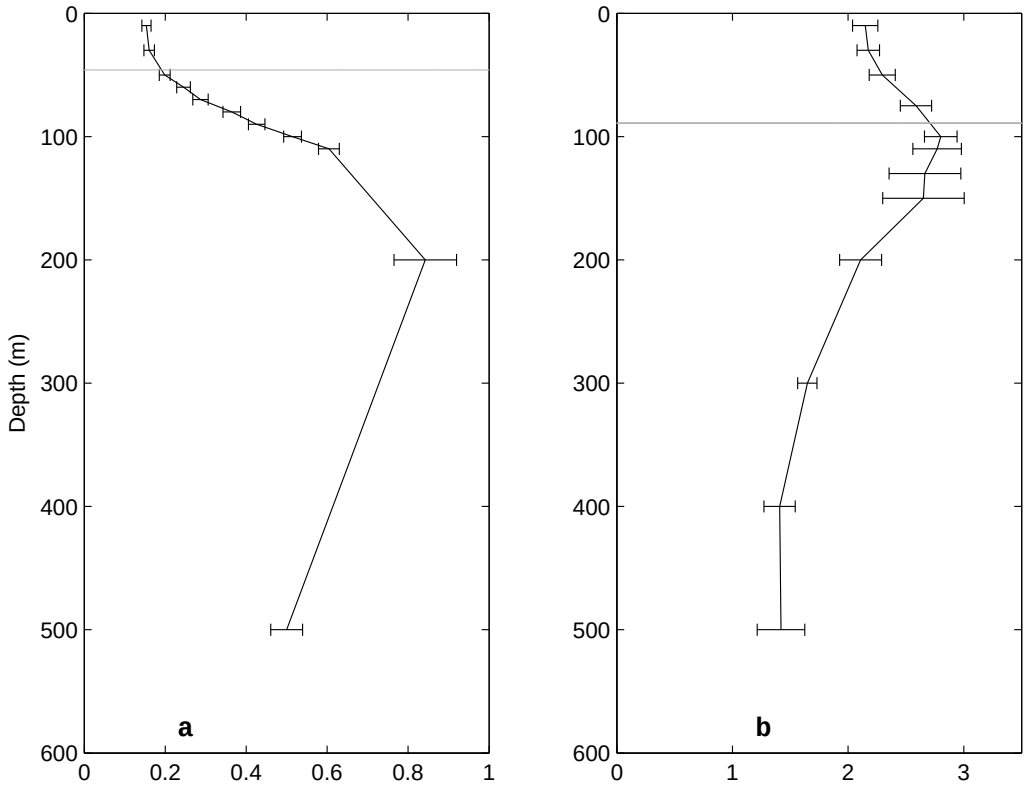

Figure 4.5: Mean iron profiles in the Ona Basin for (a) LMG0402 and (b) NBP0606. Gray horizontal lines indicate typical mixed layer depth as determined by Dong et al. (2008).

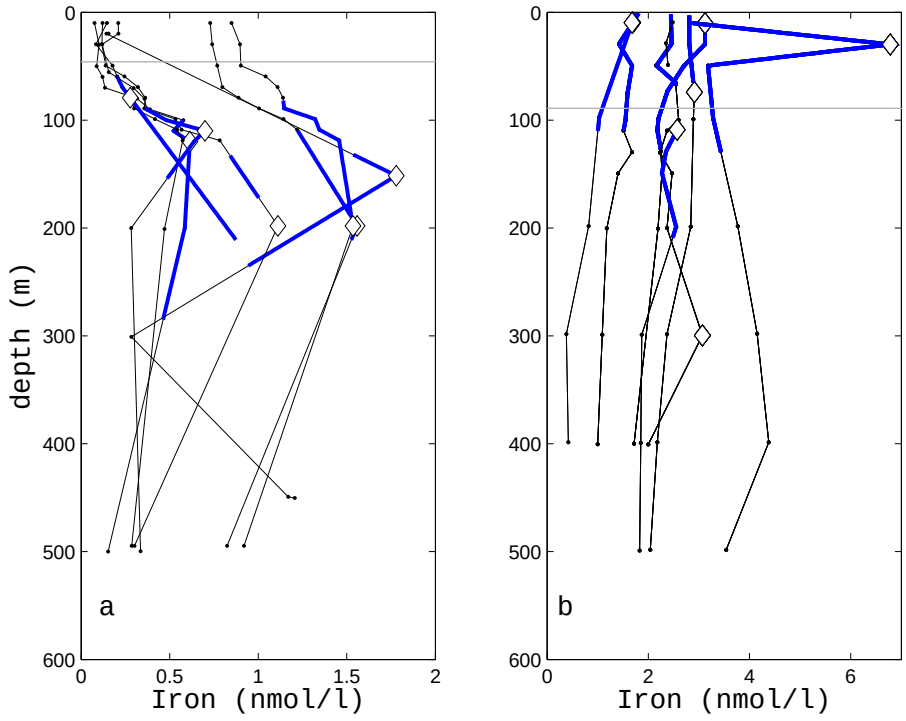

Figure 4.6: Profiles of iron near the continental shelf for (a) March 2004 (LMG0402) and (b) August 2006 (NBP0606). Gray horizontal lines indicate typical mixed-layer depth as determined by Dong et al. (2008), and segments shaded in blue indicate the depth range of the $27.5 \leq \sigma_\theta \leq 27.6$ density layer. Diamonds indicate the iron maximum at each individual station.

with iron being entrained on the shelf and transported along a subducting isopycnal into the Ona Basin. Because the isopycnal deepens to below the mixed layer as it moves off-shore, some form of vertical mixing is then needed to supply the iron into the mixed layer in the basin.

Iron profiles for stations near the continental shelf south of the Ona Basin are shown in Figure 4.6. The LMG0402 shelf profiles have a very similar structure to the Ona Basin profiles, with highest concentrations at the same depth range. The shelf profiles for NBP0606 show concentration peaks spread more broadly over the entire

water column, but the concentrations in the 100-200 m depth range are comparable to the values north of the shelf. The difference between the two cruises is consistent with higher stratification during the summer, which inhibits diapycnal mixing and helps preserve the vertical structure of the iron distribution while iron is advected off the shelf. In addition, the $27.5 \leq \sigma_\theta \leq 27.6$ isopycnal is shallower during NBP0606, allowing for isolated storm events as well as diurnal variations in mixed-layer depth to mix more iron toward the surface. However, both sets of profiles are consistent with a scenario in which horizontal advection along the isopycnal leads to high concentrations of iron below the mixed layer in the Ona Basin.

Circulation in the Ona Basin is characterized by deep mesoscale eddies that trap water (Brandon et al., 2004; Barré et al., 2008). Argo float data studied by Barré et al. (2008) showed that floats released in the Ona Basin in March 2002 and December 2003 remained in the basin for periods of 6 months to two and a half years. These numbers suggest that iron entrained near the shelf and advected into the Ona Basin during the winter months can be retained in the basin until the summer, producing the persistent peaks seen in Figures 4.3 and 4.5.

4.4 Assessing the effects of horizontal advection from satellite altimetry

Our analysis of the satellite data has focused on the deep off-shore region in the Ona Basin shown as quadrangle a in Figure 4.1. The surface waters in this region are a mixture of Antarctic Surface Water (ASW) and Winter Water (WW) associated with the ACC, and denser shelf waters propagating off-shore from the Antarctic Peninsula and the South Shetland Islands. (Zhou et al., 2010b; Barré et al., 2008). The shelf waters are iron-replete, while the ACC waters to the north of the front are iron-limited (Hopkinson et al., 2007). As the mean position of the SACCF-n moves farther off-shore, it allows some of the shelf waters to move with it, mixing with the ASW and WW in the Ona

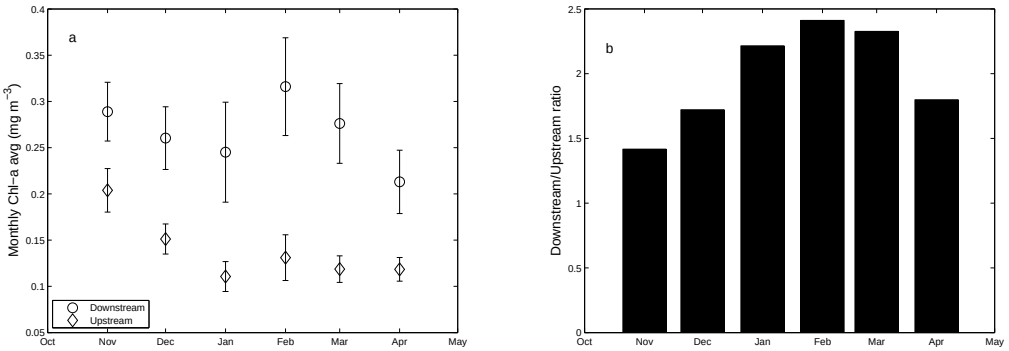

Figure 4.7: Monthly mean Chl-a concentrations (a) and concentration ratios (b) downstream and upstream of the Shackleton Transverse Ridge.

Basin, as shown in Figures 2.7 and 2.8 in Chapter 2.

For every month in our 13-year time series, we determined the fraction of all grid points in the analysis region for which SSH was less than 64 cm. SSH values in the study area increase from south to north, with the 64-cm contour identifying the location of the SACCF-n according to the criteria defined by Sokolov and Rintoul (2009). Therefore, choosing the SSH points below the 64-cm contour allowed us to estimate the proportion of shelf waters relative to ASW and WW in the analysis region, accounting for both the waters being advected off-shore behind the SACCF-n, and for eddies potentially being generated by the front to the north of it. As the proportion of iron-rich shelf water increases, the amount of iron to the Ona Basin should also increase. To examine the effect of iron advection on the Chl-a levels in the analysis region, we computed the correlation coefficients between the mean monthly Chl-a concentrations and the proportion of shelf waters in the region. For comparison, we also consider Chl-a concentrations in the low-iron, low Chl-a region to the west of the STR (quadrangle b in Figure 4.1). This region is located entirely north of SACCF-n, and our analysis in Chapter 2 has shown it to be dominated by the waters of the ACC, with little or no shelf waters present.

The difference in biological productivity between the low-iron region upstream

of the STR and the Ona Basin region downsream is illustrated in Figure 4.7. Panel a shows monthly mean Chl-a concentrations in the upstream and downstream regions outlined in Figure 4.1, and panel b shows the ratio of downstream to upstream Chl-a. For all months, the Chl-a concentrations are higher in the downstream region, where SACCF-n has moved off-shore. Downstream Chl-a levels become slightly higher from January to February before decreasing again, and the concentrations for February and March are comparable to the concentration in November, suggesting the presence of a steady supply of iron to sustain the bloom throughout the summer. Upstream concentrations decrease from November to January as the winter stock of iron is depleted, then remain low for the rest of the summer as no new iron is supplied. The differences between the two regions are largest in January, February and March, when the downstream Chl-a values rise to more than twice the upstream levels. Figure 4.8 shows the monthly correlation coefficients between Chl-a concentration and the proportion of shelf waters present in the downstream region. The coefficients are highest in November and December, exceeding the 95% confidence level, then sharply decrease in January and remain low through the rest of the summer. This decrease in correlation, combined with the persistently high Chl-a concentrations from January through March, is consistent with a scenario in which horizontal off-shore advection is a major factor in determining the strength of the Ona Basin bloom in the spring, but is not sufficient to maintain the bloom through the end of the summer.

4.5 Assessing vertical mixing from *in situ* data

4.5.1 Diapycnal mixing and mixed-layer entrainment

The results of Section 4.4 indicate that additional mechanisms of iron supply are needed to explain the persistence of the bloom from January through the end of March, when horizontal advection alone is not sufficient to maintain the Chl-a concentrations. These mechanisms can potentially be driven by both physical and biological processes.

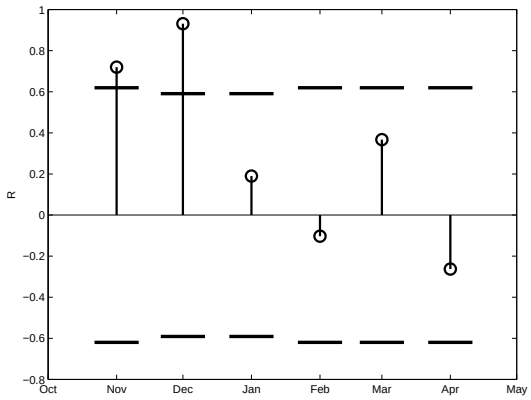

Figure 4.8: Monthly correlation coefficients between the location of the northern branch of the SACCF and the mean Chl-a levels in the Ona Basin. Heavy black lines represent the 95% confidence interval

Laboratory studies have found that remineralization of particulate iron and recycling by microzooplankton grazing can play a significant role in supplying bioavailable iron to phytoplankton (Barbeau et al., 2001; Dalbec and Twining, 2009), and *in situ* studies during iron enrichment experiments in the Southern Ocean have shown that these processes can account for over 30% of the iron supply in the euphotic zone (Bowie et al., 2001; Strzepek et al., 2005). The determination of biogeochemical effects on the iron concentrations in our study region is beyond the scope of this dissertation. Therefore, we focus our analysis on the physical processes, with the goal of determining if physical mechanisms alone can supply sufficient iron to the mixed layer to sustain a bloom. One possible mechanism is diapycnal mixing, which has been shown to be elevated over regions of rough bathymetry throughout the Southern Ocean (Sloyan, 2005). Fine-scale estimates of diapycnal diffusivity κ from LADCP and XCTD profiles in Drake Passage indicate the presence of enhanced mixing, with values of κ ranging from $O(10^{-4})$ to $O(10^{-3})$ m^2 s^{-1} (Naveira Garabato et al., 2004; Thompson et al., 2007). These estimates are consistent with recent microstructure and tracer diffusion estimates in Drake Passage, showing values of κ ranging from 1×10^{-4} m^2 s^{-1} to 3×10^{-4} m^2 s^{-1}. (L. St.

Laurent, 2011, personal communication)

Given these diffusivity estimates and the mean Ona Basin iron profiles in Figure 4.5, and assuming no horizontal advection, the vertical diffusive flux F_z of iron can be computed as

$$F_z = -\kappa \frac{\partial Fe}{\partial z}. \tag{4.1}$$

Solving this equation for the averaged profiles shown in Figure 4.5 and a diffusivity of κ=1.1$\times 10^{-4}$ m^2 s^{-1} gives an estimated iron flux of 96$\pm$9 nmol m^{-2} day^{-1} upward from the iron maximum into the base of the winter mixed layer and 64$\pm$2 nmol m^{-2} day^{-1} into the base of the summer mixed layer. The difference between the seasons is due to the higher iron gradients in winter, as seen in the upper 150 m in figures 2.3 and 4.5.

Changes in mixed-layer depth provide an additional mechanism for increasing iron concentrations near the surface. As the mixed layer deepens, it entrains iron from the top of the pycnocline and mixes it toward the surface. This additional entrainment can help compensate for decreasing iron concentrations and reduced near-surface gradients as iron is consumed over the summer.

Figure 4.9 shows monthly mean estimates of Ona Basin mixed-layer depth for the months of November through April, based on a global climatology by de Boyer Montegut et al. (2004) and a Southern Ocean climatology by Dong et al. (2008). In addition, estimates based on CTD data sampled during LMG0402 are shown for the months of February and March. Both climatologies use two property-difference criteria for determining mixed-layer depth, one based on density and one on temperature. The density-based criterion defined the base of the mixed layer as the depth at which the potential density increased by 0.03 kg m^{-3} relative to the value at 10 m. The temperature criterion was based on the depth where the absolute change in potential temperature was 0.2°C. We used the same criteria to compute the LMG0402 estimates.

In November and December, when correlations between SACCF-n position and Chl-a concentration are highest, the mixed layer shallows, indicating that entrainment

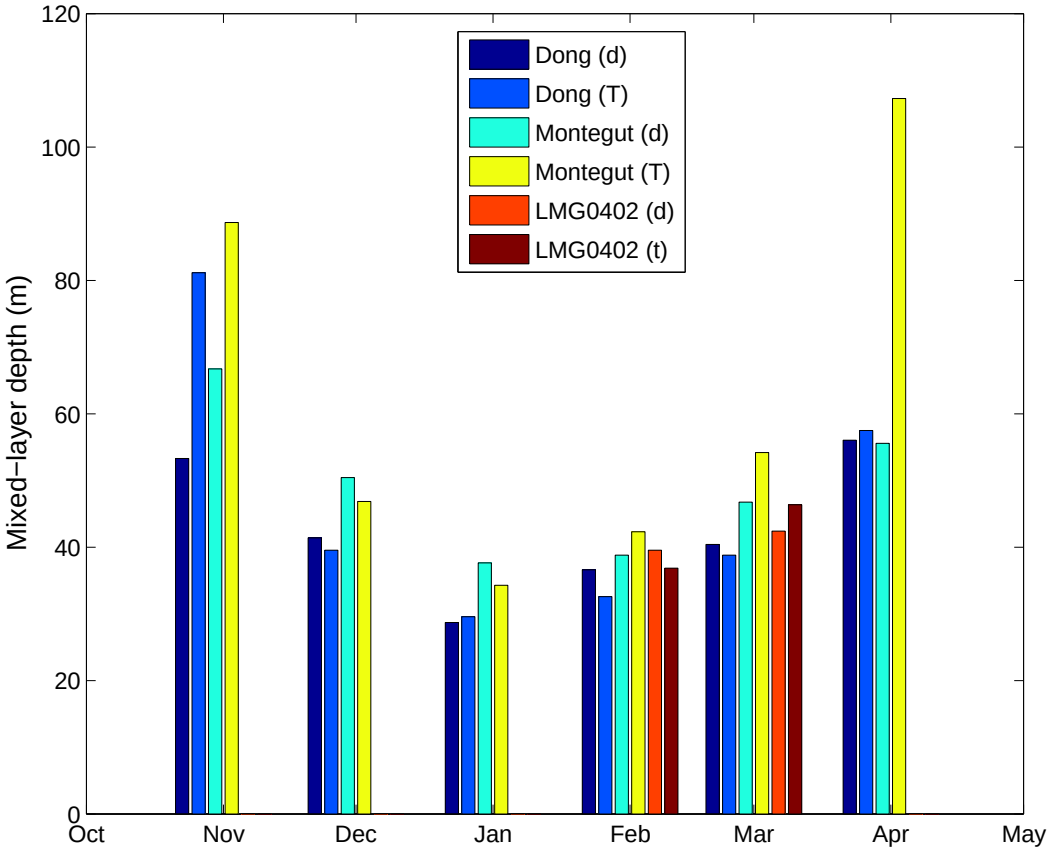

Figure 4.9: Monthly mixed-layer depths in the Ona Basin, based on the Dong et al. (2008) Southern Ocean climatology, the de Boyer Montegut et al. (2004) global climatology, and the CTD data collected during LMG0402. Estimates based on both the density (d) and temperature (t) criteria are shown.

is unlikely to supply iron to the euphotic zone. Starting in January and continuing until the end of the summer, the mixed layer deepens as the correlations between frontal position and Chl-a decrease, and the high Chl-a levels persist. This pattern is consistent with a scenario in which mixed-layer entrainment provides the additional iron needed to sustain the bloom in the Ona Basin during the months when horizontal advection no longer explains the persistence of the bloom.

Given the monthly mixed-layer depth changes seen in Figure 4.9 and the mean iron profiles in Figure 4.5, it is possible to estimate a mean daily entrainment rate for iron into the base of the mixed layer. The total amount A of dissolved iron in a column of water in the mixed layer can be calculated as

$$A = \int_0^h Fe\, dz, \tag{4.2}$$

where h is the mixed-layer depth. The mean iron concentration throughout the mixed layer can then be calculated as Fe_{ml}=A/h. The mean daily entrainment rate over a period of n days can be calculated as

$$(Fe_{ml}(n) - Fe_{ml}(1))/n, \tag{4.3}$$

where $Fe_{ml}(i)$ is the mixed-layer iron concentration on the ith day.

If we assume that the mixed-layer changes steadily and monotonically over the course of each month, then applying 4.3 to the mixed-layer depths shown in Figure 4.9 yields daily entrainment rates ranging from 5 to 25 nmol m^{-2} day$^{-}1$. However, such an assumption does not reflect the diurnal mixed layer cycle or the impact of isolated storm events that may cause large changes in the mixed-layer depth over a short period of time. In the next section, we use a one-dimensional numerical model to take these additional variables into account.

4.5.2 Results from one-dimensional model simulation

The daily iron requirements to sustain a bloom in the Ona Basin have not been determined; however, similar studies in the Bransfield Strait (Ardelan et al., 2010) and the Kerguelen Plateau (Blain et al., 2007) estimated the iron requirements at approximately 286 nmol m^{-2} day^{-1} and 208 nmol m^{-2} day^{-1}, respectively. Given these requirements and the estimates made in the previous two sections, neither diapycnal mixing nor mixed-layer entrainment alone would be sufficient to sustain the Ona Basin Chl-a levels during the late summer months. Therefore, it is necessary to consider the combined effect of both processes on the mixed-layer iron supply, along with the short-term variability of the mixed layer. To evaluate these effects, we performed a numerical simulation using a modified version of the one-dimensional mixed-layer model by Price et al. (1986, henceforth PWP).

The PWP model was originally developed to compute the diurnal variability of the mixed-layer depths. It accepts a time series of forcing variables consisting of winds, precipitation and surface heat fluxes, and applies them to mix initial profiles of temperature and salinity. For our analysis, we modified the model to accept an additional input of an initial iron profile, created from the averaged profile shown in Figure 4.5a by using a linear fit to interpolate the data to 5 m resolution. The initial temperature and salinity profiles, made by averaging all available LMG0402 profiles in the Ona Basin and also interpolated to 5 m resolution, are shown in Figure 4.10. Our simulation was run for 120 days, with a time step of 10 minutes and a depth increment of 5 m, to a maximum depth of 500 m, as most of the iron profiles were not sampled below that depth.

To account for diapycnal mixing, we modified PWP to incorporate the vertical diffusive flux of iron as defined in Equation 4.1. The modified model solved for F_z at each time step, with boundary conditions $\frac{\partial Fe}{\partial z}$=0 and $\frac{\partial^2 Fe}{\partial z^2}$=0 to ensure no flux at the bottom of the water column or through the base of the mixed layer. We then ran the model for two scenarios: one without the flux modification, to yield an estimate of

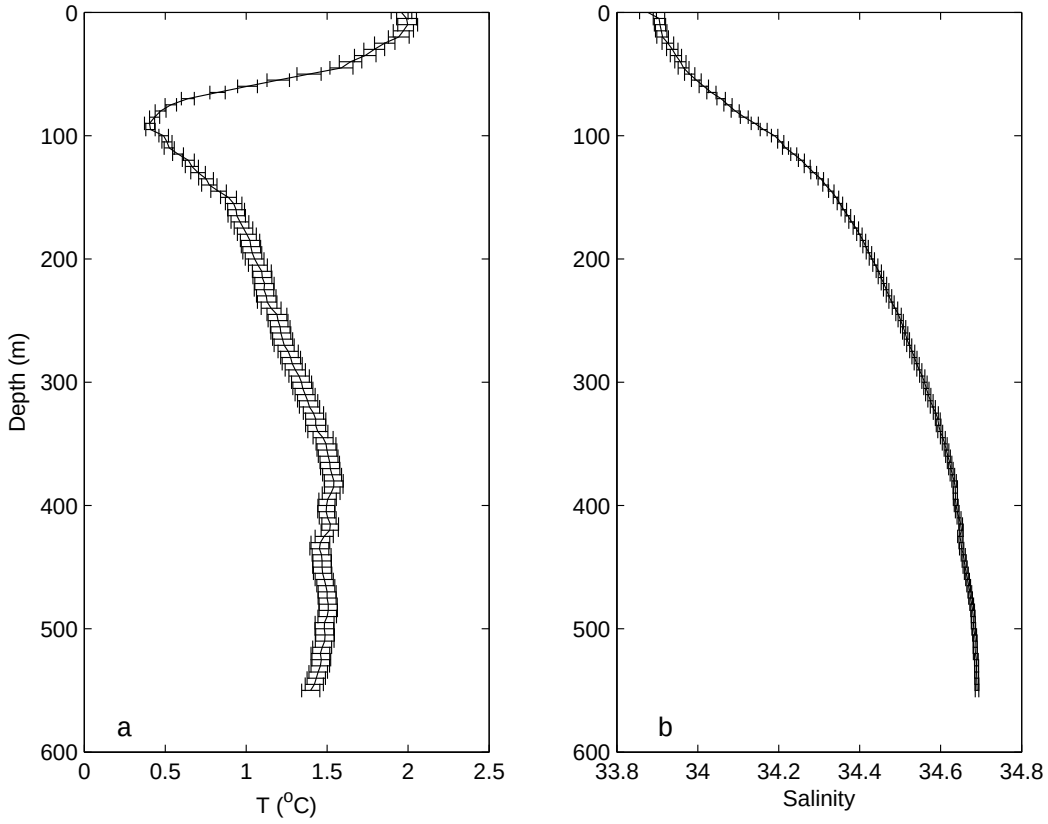

Figure 4.10: (a) Temperature and (b) salinity profiles used as inputs for the PWP model.

mixed-layer iron concentrations based only on entrainment; and one using the modified model to provide an estimate diapycnal mixing and entrainment combined.

To determine the uncertainties for our results, we performed a Monte Carlo simulation in which the PWP model was run 100 times for each of the two scenarios described above. For each the original iron input was perturbed by a vector of normally distributed random numbers scaled to match the mean standard deviation of the iron profiles shown in Figure 4.5a. We then computed the mean daily entrainment of iron for each run, and used the standard deviation of the result as the uncertainty for our original estimate.

The results of the simulation for the combined mixing and entrainment scenario

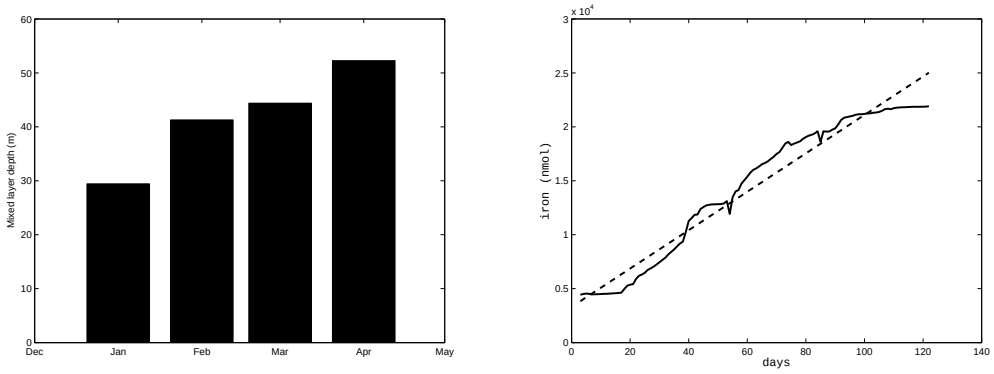

Figure 4.11: Averaged monthly mixed layer depth (a) and averaged daily iron concentration in the top 30 m (b), as computed by the PWP model. The dashed line in (b) represents the linear fit used to calculate the daily entrainment rate.

are shown in Figure 4.11. The averaged monthly mixed-layer depths are comparable to the climatology-derived depths shown in Figure 4.9, as well as observed depths from LMG0402. The solid curve in panel b shows the mean daily iron concentration found in the top 30 m of the water column after both mixing and entrainment have taken place. The mean daily entrainment rate, based on the linear fit illustrated by the dashed line in Figure 4.11, is 174$\pm$44 nmol m^{-2} day^{-1}. The entrainment-only simulation produced a mean daily entrainment rate of 12$\pm$9 nmol m^{-2} day^{-1}, consistent with the rates derived from the mixed layer estimates in Section 4.5.1.

The mixing and entrainment processes discussed in the preceding sections are purely physical, and do not take into account the biogechemical mechanisms on mixed-layer iron supply. However, the results of our numerical simulation indicate that physical processes alone can potentially deliver iron into the mixed layer at a rate exceeding 200 nmol m^{-2} day^{-1} during the summer. Therefore, the physical processes in the Ona Basin appear sufficient to sustain the summer bloom for as long as the near-surface iron gradients persist, even without additional contribution from grazing and remineralization.

4.6 Summary

Satellite-derived Chl-a concentrations from November through April are consistently higher in the waters to the east of the Shackleton Transverse Ridge than in the waters to the west. The northern branch of the Southern ACC Front, as defined by the 64-cm sea-surface height contour, moves off-shore east of the ridge, allowing for horizontal advection of iron-rich shelf waters into the Ona Basin. Comparison between sea-surface height and Chl-a data shows that the proportion of shelf waters present in the Ona Basin is highly correlated with Chl-a concentration during the months of November and December. The correlations become smaller from January onward, while Chl-a levels in the Ona Basin rise slightly, and the ratio of mean Chl-a east of the ridge to mean Chl-a west of the ridge increases. These results are consistent with a scenario in which horizontal advection of shelf waters can account for the intensity of the spring bloom in the Ona Basin, but this advection alone is not sufficient to sustain the bloom through the end of the summer.

Iron profiles in the Ona Basin during both winter 2006 and summer 2004 show a strong subsurface maximum between 100 and 200 m, and high near-surface gradients that persist from winter into summer, allowing for an iron flux to the base of the mixed layer due to diapycnal mixing. The mixed layer in the Ona Basin also deepens from January into April, after becoming shallower from November to January. The increased mixed-layer depth provides an additional supply of iron to the surface, by allowing it to be entrained from the top of the pycnocline. Estimates of the mean daily entrainment rate and the mixing-induced iron flux indicate that neither process alone is sufficient to sustain the the summer bloom in the Ona Basin. However, a numerical simulation suggests that the combination of the two processes can supply enough iron into the top 30 m of the basin to sustain the bloom. The simulation does not take into account the biochemical mechanisms that can also affect mixed-layer iron concentrations, or the effects of eddy-driven and wind-driven upwelling. A comprehensive estimate of the mixed-layer iron budget will need to take these additional processes into account.

Appendix A

Computing Chi-square estimator to assess the optimal number of source waters for OMP analysis

The chi-square distribution for the output of OMP analysis for a normally-distributed variable r can be defined as

$$\chi^2 \equiv \sum_{i=1}^{m} \left(\frac{r_i}{\sigma_i} \right)^2 \tag{A.1}$$

where m and r are defined as in 2.3 and σ_i is the standard deviation of each parameter measured at the station (Press et al., 1986). For values of σ_i for every at each individual station, we used the standard deviation of that parameter within the dominant water mass at that station, computed using the same method as the standard deviations used to compute the weights in 2.3.2

For a given number of degrees of freedom ν, we compute the probability that the data will not exceed a given value of χ^2 by chance, with higher probability indicating a higher chance that the end point definitions represent the source waters mixing into the region. This probability can be computed as the incomplete gamma function $Q(0.5 \times \nu, 0.5 \times \chi^2)$. (Press et al., 1986) For the distribution computed here, ν is the number of

stations used in the OMP analysis minus the number of columns in matrix G.

References

Abraham, E. R., Law, C. S., Boyd, P. W., Lavender, S. J., Maldonado, M. T., and Bowie, A. R., 2000: Importance of stirring in the development of an iron-fertilized phytoplankton bloom. *Nature*, **407**, 727–729.

Ardelan, M. V., Holm-Hansen, O., Hewes, C. D., Reiss, C. S., Silva, N. S., Dulaiova, H., Steinnes, E., and Saksahaug, E., 2010: Natural iron enrichment around the Antarctic Peninsula in the Southern Ocean. *Biogeosciences*, **7**, 11–25.

Barbeau, K., Kujawinski, E. B., and Moffett, J. W., 2001: Remineralization and recycling of iron, thorium and organic carbon by heterotrophic marine protists in culture. *Aquat. Macrob. Ecol.*, **24**, 69–81.

Barré, N., Provost, C., Sennechael, N., and Lee, J. H., 2008: Circulation in the Ona Basin, southern Drake Passage. *J. Geophys Res.*, **113**. C04033,doi: 10.1029/2007JC004549.

Bendat, J. S., and Piersol, A. G., 2000: *Random Data: Analysis and Measurement Procedures.* John Wiley and Sons Ltd, 3rd edition. 594 pages.

Blain, S., Queguiner, B., Armand, L., Belviso, S., Bombled, B., Bopp, L., Bowie, A., Brunet, C., Brussaard, C., Crlotti, F., Christaki, U., Corbiere, A., and Durand, I., 2007: Effect of natural iron fertilization on carbon sequestration in the Southern Ocean. *Nature*, **446**, 1070–1074.

Blain, S., Treguer, P., Belviso, S., Bucciarelli, E., Denis, M., Desabre, S., Fiala, M., Jezequel, V. M., Le Fevre, J., Mayzaud, J. C., P. Marty, and Razouls, S., 2001: A biogeochemical study of the island mass effect in the context of the iron hypothesis: Kerguelen Islands, Southern Ocean. *Deep-Sea Res. I*, **48**, 163–187.

Bowie, A. R., Maldonado, M. T., Frew, R. D., Croot, P. L., Achterberg, E. P., Mantonura, R. F. C., Worsfold, P. J., Law, C. S., and Boyd, P. W., 2001: The fate of added iron during a mesoscale fertilisation experiment in the Southern Ocean. *Deep-Sea Res. II*, **48**, 2703–2743.

Boyd, P. W., 2002: The Role of iron in the biogeochemistry of the Southern Ocean and equatorial Pacific: A comparison of in situ iron enrichments. *Deep-Sea Res. II*, 1803–1821.

Brandon, M. A., Naganobu, M., Demer, D. A., Chernyshkov, P., Trathan, P. N., Thorpe, S. E., Kameda, T., Berezhinskiy, O. A., Hawker, E., and Grant, S., 2004: Physical oceanography in the Scotia Sea during the CCAMLR 2000 survey, austral summer 2000. *Deep-Sea Res. II*, **51**, 1301–1321.

Broecker, W. S., and Henderson, G. M., 1998: The Sequence of events surrounding Termination ii and their implications for the causes of Glacial Interglacial CO_2 Changes. *Paleoceanography*, **13**, 352–364.

Budillon, G., Pacciaroni, M., Cozzi, S., Rivaro, P., Catalano, G., Ianni, C., and Cantoni, C., 2003: An optimum multiparameter mixing analysis of the shelf waters in the Ross Sea. *Antarctic Science*, **15**, 105–118.

Chisholm, S. W., and Morel, F. M. M., 1991: What controls phytoplankton production in nutrient-rich areas of the open sea? *Limnol. and Oceanogr.*, **36**, 1507–1511.

Crawford, W., 1986: A comparison of length scales and decay times of turbulence in stably stratified flows. *J. Phys. Oceanogr.*, **16**, 1847–1854.

Dalbec, A. A., and Twining, B. S., 2009: Remineralization of bioavailable iron by a heterotropic dinoflagellate. *Aquat. Microb. Ecol.*, **54**, 279–290.

de Baar, H. J. W., and de Jong, J. T. M., 2001: *Distributions, Sources and Sinks of Iron in Seawater*, 123–253. John Wiley and Sons Ltd.

de Baar, H. J. W., de Jong, J. T. M., Bakker, D. C. E., Loscher, B. M., Veth, C., Bathmann, U., and Smetacek, V., 1995: Importance of iron for plankton blooms and carbon dioxide drawdown in the southern ocean. *Nature*, **373**, 412–415.

de Boyer Montegut, C., Madec, G., Fischer, A. S., Lazar, A., and Iudicone, D., 2004: Mixed layer depth over the global ocean: an examination of profile data and a profile-based climatology. *J. Geophys. Res.*, **109**. DOI: 10.1029/2004JC002378.

de Brauwere, A., Jacquet, S. H. M., De Ridder, F., Dehairs, F., Pintelon, R., Schoukens, J., and Baeyens, W., 2007: Water mass distributions in the Southern Ocean derived from a parametric analysis of mixing water masses. *J. Geophys. Res.*, **112**. C02021, doi:10.1029/2006JC003742.

Dillon, T. M., 1982: Vertical overturns: a comparison of Thorpe and Ozmidov scales. *J. Geophys. Res.*, **87**, 9601–9613.

Dong, S., Sprintall, J., Gille, S. T., and Talley, L., 2008: Southern Ocean mixed-layer depth from Argo float profiles. *J. Geophys. Res.*, **113**. C06013, DOI:10.1029/2006JC004051.

Ducet, N., Le Traon, P.-Y., and Reverdin, G., 2000: Global high resolution mapping of ocean circulation from Topex/Poseidon and ERS-1 and -2. *J. Geophys. Res.*, **105**, 19477–19498.

Eckart, C., 1948: An analysis of the stirring and mixing processes in incompressible fluids. *J. Mar. Res.*, **7**, 265–275.

Efron, B., and Gong, G., 1983: A leisurely look at the bootstrap, the jackknife, and cross-validation. *Amer. Stat.*, **37**, 36–48.

Galbraith, P. S., and Kelley, D. E., 1996: Identifying overturns in CTD profiles. *J. Atmos. Oceanic Technol.*, **13**, 688–702.

Gargett, A., and Garner, T., 2008: Determining Thorpe scales from ship-lowered CTD density profiles. *J. Atmos. Oceanic Technol.*, **25**, 1657–1670. DOI: 10.1175/2008JTECHO541.1.

Garrett, C., and Munk, W., 1975: Space-time scales of internal waves – Progress report. *J. Geophys. Res.*, **80**, 291–297.

Gille, S. T., Lombrozo, A., Sprintall, J., Stephenson, G., and Scarlet, R., 2009: Anomalous spiking in spectra of XCTD temperature profiles. *J. Atmos. Oceanic Technol.*, **26**, 1157–1164.

Gouretski, V. V., and Koltermann, K. P., 2004: Woce global hidrographic climatology. Tech. rep. 35/2004, Berichte des Bundesamtes fur Seeschifffahrt und Hydrographie, Hamburg, Germany.

Gregg, M. C., 1987: Diapycnal mixing in the thermocline: A review. *J. Geophys. Res.*, **92**, 5249–5286.

Gregg, M. C., and Kunze, E., 1991: Internal wave shear and strain in Santa Monica basin. *J. Geophys. Res.*, **96**, 16709–16719.

Helbling, E. W., Villafane, V., and Holm-Hansen, O., 1991: Effect of iron on productivity and size distribution of Antarctic phytoplankton. *Limnol. and Oceanogr.*, **36**, 1879–1885.

Hewes, C., Reiss, C. S., and Holm-Hansen, O., 2009: A quantitative analysis of sources for summertime phytoplankton variability over 18 years in the South Shetland Islands (Antarctica) region. *Deep-Sea Res. I*, **56**, 1230–1241.

Hewes, C. D., Reiss, C. S., Kahru, M., Mitchell, B. G., and Holm-Hansen, O., 2008: Control of phytoplankton biomass by dilution and mixed layer depth in the western weddell-scotia confluence (WSC). *Mar. Ecol. Prog. Ser.*, **366**, 15–29.

Heywood, K. J., Naveira Garabato, A. C., and Stevens, D. P., 2002: High mixing rates in the abyssal southern ocean. *Nature*, **415**, 1011–1014.

Hofmann, E. E., Klinck, J. M., and Lascara, D. A., C. M.and Smith, 1996: *Water mass distribution and circulation west of the Antarctric Peninsula and including Bransfield Strait*, volume 70, 61–80. American Geophysical Union, Washington, D.C.

Holm-Hansen, O., Kahru, M., and Hewes, C. D., 2005: Deep chlorophyll a maxima (DCMSs) in pelagic Antarctic waters. II. Relation to bathymetric features and dissolved iron concentrations. *Mar. Ecol. Prog. Ser.*, **297**, 71–81.

Holm-Hansen, O., Kahru, M., Hewes, C. D., Kawaguchi, S., Kameda, T., Sushin, V., Krasovski, I., Priddle, J., Korb, R., Hewitt, R. P., and Mitchell, B. G., 2004: Temporal and spatial distribution of chlorophyll-a in surface waters of the Scotia Sea as determined by both shipboard measurements and satellite data. *Deep-Sea Res. II*, **51**, 1323–1331.

Hopkinson, B. M., Mitchell, G. B., Reynolds, R. A., Wang, H., Measures, C. I., Selph, K. E., Hewes, C. D., Holm-Hansen, O., and Barbeau, K. A., 2007: Iron limitation across chlorophyll gradients in the southern Drake Passage: Phytoplankton responses to iron addition and photosynthetic indicators of iron stress. *Limnol. and Oceanogr.*, **52**, 2540–2554.

Hoppema, M., and Goeyens, L., 1999: Redfield behavior of carbon, nitrogen and phosphorus depletions in antarctic surface water. *Limnol. and Oceanogr.*, **44**, 220–224.

Houk, R. S., and Thompson, J. J., 1988: Inductively coupled plasma mass spectrometry. *Mass Spectrom. Revs.*, **7**, 425–461.

Hughes, C. W., and Ash, E., 2001: Eddy forcing of the mean flow in the Southern Ocean. *J. Geophys. Res.*, **106**, 2713–2722.

Kahru, M., Mitchell, B. G., Gille, S. T., Hewes, C. D., and Holm-Hansen, O., 2007: Eddies enhance biological production in the Weddell-Scotia Confluence of the Southern Ocean. *Geophys. Res. Lett.*, **34**. L14603, doi:10.1029/2007GL030430.

Kalnay, E., and coauthors, 1996: The NCEP/NCAR 40-year reanalysis project. *Bullet. Amer. Meteorol. Soc.*, **77**, 437–471.

Karstensen, J., and Tomczak, M., 1998: Age determination of mixed water masses using CFC and oxygen data. *J. Geophys. Res.*, **103**, 18599–18609.

Karstensen, J., and Tomczak, M., 2005: OMP analysis package for Matlab vesion 2.0. http://www.ldeo.columbia.edu/~jkarsten/omp_std/README.html. Lamont-Doherty Earth Observatory.

Kunze, E., 2003: Yes, we have no abyssal mixing. In *Near-Boundary Processes and Their Parameterizations: Proc. 'Aha Huliko'a Hawaiian Winter Workshop*, 85–93. University of Hawaii at Manoa.

Kunze, E., Firing, E., Hummon, J. M., Chereskin, T. K., and Thurnherr, A., 2006: Global abyssal mixing inferred from lowered adcp shear and ctd strain profiles. *J. Phys. Oceanogr.*, **36**, 1553–1576.

Lapeyre, G., and Klein, P., 2006: Impact of the small-scale elongated filaments on the oceanic vertical pump. *J. Mar. Res.*, **64**, 835–851.

Ledwell, R. R., St.Laurent, L. C., Girton, J. B., and Toole, J. M., 2011: Diapycnal mixing in the Antarctic Circumpolar Current. *J. Phys. Oceanogr.*, **41**. DOI10.1175/2010JPO4557.1.

Lenn, Y.-D., Chereskin, T. K., Sprintall, J., and Firing, E., 2007: Mean jets, mesoscale variability and eddy momentum fluxes in the surface layer of the Antarctic Circumpolar Current in Drake Passage. *J. Mar. Res.*, **66**, 27–58.

Lipsky, J. D., 2004: AMLR 2003/2004 field season report: objectives, accomplishments and tentative conclusions. Technical Report NOAA-TM-NMFS-SWFSC-367, National Oceanic and Atmospheric Administration.

Maraldi, C., Mongin, M., Coleman, R., and Testut, L., 2009: The influence of lateral mixing on a phytoplankton bloom: Distribution in the Kerguelen Plateau region. *Deep Sea Res. I*, **56**, 963–973.

Martin, J., Gordon, R., and Fitzwater, S., 1990: Iron in Antarctic waters. *Nature*, **345**, 156–158.

Martin, J. P., and Rudnick, D. L., 2007: Inferences and observations of turbulent dissipation and mixing in the upper ocean at the hawaiian ridge. *J. Phys. Oceanogr.*, **37**, 476–494.

Measures, C. I., Landing, W. M., Brown, M. T., and S., B. C., 2008: A commercially available rosette system for trace metal clean sampling. *Limnol. and Oceanogr. methods*, **6**, 384–394.

Measures, C. I., Yuan, J., and Resing, J. A., 1995: Determination of iron in seawater by flow injection analysis using in-line preconcentration and spectrophotometric detection. *Marine Chem.*, **50**, 3–12.

Morrison, J., Andersen, R., Larson, N., D'Asaro, E., and Boyd, T., 1994: The correction for thermal lag effects in Sea-Bird CTD data. *J. Atmos. Oceanic Technol.*, **11**, 1151–1164.

Munk, W. H., 1966: Abyssal recipes. *Deep-Sea Res.*, **13**, 207–230.

Naveira Garabato, A. C., Polzin, K. L., King, B. A., Heywood, K. J., and Visbeck, M., 2004: Widespread intense turbulent mixing in the Southern Ocean. *Science*, **303**, 210–213.

Niiler, P. P., Amos, A., and Hu, J., 1991: Water masses and 200 m relative geostrophic circulation in the western Bransfield Strait region. *Deep-Sea Res. I*, **38**, 943–959.

O'Reilly, J. E., Maritorena, S., Mitchell, B. G., Siegel, D. A., Carder, K. L., Garver, S. A., Kahru, M., and McClain, C., 1998: Ocean color chlorophyll algorythms for SeaWiFS. *J. Geophys. Res.*, **103**, 24,937–24,953.

Orsi, A. H., Whitworth, T., and Nowlin, W. D., 1995: On the meridional extent and fronts of the Antactic Circumpolar Current. *Deep-Sea Res. I*, **42**, 641–673.

Ozmidov, R. V., 1965: On the turbulent exchange in a stably stratified ocean. *Izv. Acad. Sci. USSR, Atmos. Oceanic Phys.*, **1**, 861–871.

Planquette, H., Statham, P. J., Fones, G. R., and Sanders, R., 2006: Evidence of a natural iron source around the Crozet Islands, Southern Ocean. In *Fall Meet. Supplement*. AGU. Abstract OS32B-03.

Press, W. H., Flanner, B. P., Teukolsky, S. A., and Vetterling, W. T., 1986: *Numerical Recipes: The Art of Scientific Computing*, chapter 14, 502–504. Cambridge University Press.

Price, J. F., Weller, R. A., and Pinkel, R., 1986: Diurnal cycling: Observation and models of the upper ocean response to diurnal heating, cooling and wind mixing. *J. Geophys. Res.*, **91**, 8411–8427.

Redfield, A. C., Ketchum, B. H., and Richards, F. A., 1963: *The influence of organisms on the composition of sea-water*, volume 2, 26–77. John Wiley and Sons Ltd.

Sea-Bird Electronics, Inc., 2009: *SEASOFT-Win32: SBE Data Processing*. Sea-Bird Electronics, Inc. Available on-line at ftp://ftp.halcyon.com/pub/seabird/OUT/Older_Manuals/Software_Manuals/-SBE_Data_Processing/SBEDataProcessing_7.20a.pdf.

Silva, S. N., Helbling, E. W., Villafane, V. E., Amos, A. F., and Holm-Hansen, O., 1995: Variability in nutrient concentrations around Elephant Island, Antarctica, during 1991-1993. *Polar Res.*, **14**, 69–82.

Sloyan, B., 2005: Spatial variability of mixing in the Southern Ocean. *Geophys. Res. Lett.*, **32**. DOI: 10.10292005GL023568.

Sloyan, B. M., Talley, L. D., Chereskin, T. K., Fine, R., and Holte, J., 2010: Antarctic Intermediate Water and Subantarctic Mode Water formation in the southeast Pacific: the role of turbulent mixing. *J. Phys. Oceanogr.*, **40**. DOI:10.1175/2010JPO4114.1.

Sokolov, S., and Rintoul, S. R., 2007a: Multiple jets of the Antarctic Circumpolar Current south of Australia. *J. Phys. Oceanogr.*, **37**, 1394–1412.

Sokolov, S., and Rintoul, S. R., 2007b: On the relationship between fronts of the Antarctic Circumpolar Current and surface chlorophyll concentrations in the Southern Ocean. *J. Geophys. Res.*, **112**. C07030, doi:10.1029/2006JC004072.

Sokolov, S., and Rintoul, S. R., 2009: Circumpolar structure and distribution of the Antarctic Circumpolar Current fronts: 2. Variability and relationship to sea surface height. *J. Geophys. Res.*, **114**. C1109, doi:10.1029/2008JC005428.

Strzepek, R. F., Maldonado, M. T., Higgins, J. L., Hall, J., Safi, K., Wilhelm, S. W., and Boyd, P. W., 2005: Spinning the 'Ferrous Wheel': the importance of the microbial community in an iron budget during the FeCycle experiment. *Glob. Biogeochem. Cycles*, **19**. GB4S26, doi:10.1029/2005GB002490.

Sullivan, C. W., Arrigo, K. R., McClain, C. R., Comiso, J. C., and Firestone, J., 1993: Distribution of phytoplankton blooms in the Southern Ocean. *Science*, **262**, 1832–1837.

Thompson, A. F., Gille, S. T., MacKinnon, J. A., and Sprintall, J., 2007: Spatial and temporal patterns of small-scale mixing in Drake Passage. *J. Phys. Oceanogr.*, **37**, 572–592.

Thorpe, S. A., 1977: Turbulence and mixing in a Scottish loch. *Philos. Trans. Roy. Soc. London*, **286A**, 125–181.

Tomczak, M., 1981: A multiparameter extension of temperature/salinity diagram techniques for the analysis of non-isopycnal mixing. *Prog. Oceangr.*, **10**, 147–171.

Tomczak, M., and Large, D. G. B., 1989: Optimum multiparameter analysis of mixing in the thermocline of the Eastern Indian Ocean. *J. Geophys. Res.*, **94**, 16141–16149.

Tomczak, M., and Liefrink, S., 2005: Interannual variations of water mass volumes in the Southern Ocean. *J. Atmos. Ocean Sci.*, **10**, 31–42.

Tomczak, M., and Poole, R., 1999: Optimum multiparameter analysis of the water mass structure in the Atlantic Ocean thermocline. *Deep-Sea Res. I*, **46**, 1895–1921.

Toole, J. M., Polzin, K. L., and Schmitt, R. W., 1994: Estimates of diapycnal mixing in the abyssal ocean. *Science*, **264**, 1120–1123.

Venables, H. J., Pollard, R. T., and Popova, E. E., 2007: Physical conditions controlling the development of a regular phytoplankton bloom north of the Crozet Plateau, Southern Ocean. *Deep-Sea Res. II*, **54**, 1949–1965.

von Gyldenfeldt, A.-B., Fahrbach, E., Garcia, M. A., and Schroder, M., 2002: Flow variability at the tip of the Antarctic Peninsula. *Deep-Sea Res. II*, **49**, 4743–4766.

Whitehouse, M. J., Korb, R. E., Atkinson, A., Thorpe, S. E., and Gordon, M., 2008: Formation, transport and decay of an intense phytoplankton bloom within the High-Nutrient Low-Chlorophyll belt of the Southern Ocean. *J. Mar. Sys.*, **70**, 150–167.

Whitworth, T., Nowlin, W. D., Orsi, A. H., Locarnini, R. A., and Smith, S. G., 1994: Weddell Sea shelf water in the Bransfield Strait and Weddell-Scotia Cconfluence. *Deep-Sea Res. I*, **41**, 629–641.

Wijesekera, H., Padman, L., Dillon, T., Levine, M., Paulson, C., and Pinkel, R., 1993: The application of internal-wave dissipation models to a region of strong mixing. *J. Phys. Oceanogr.*, **23**, 269–286.

Yelland, M., Moat, B. I., Taylor, P. K., Pascal, R. W., Hutchings, J., and Cornell, V. C., 1998: Wind stress measurements from the open ocean corrected for airflow distortion. *J. Phys. Oceanogr.*, **28**, 1511–1526.

Yelland, M., and Taylor, P. K., 1996: Wind stress measurements from the open ocean. *J. Phys. Oceanogr.*, **26**, 541–558.

You, Y., and Tomczak, M., 1993: Thermocline circulation and ventilation in the Indian Ocean derived from water mass analysis. *Deep Sea Res.*, **40**, 13–56.

Zhou, M., Niiler, P. P., and Hu, J., 2002: Surface currents in the Bransfield and Gerlache Straits, Antarctica. *Deep-Sea Res. I*, **49**, 267–280.

Zhou, M., Zhu, Y., and Dorland, R., 2010a: Dynamics of the current system in the Southern Drake Passage. *Deep-Sea Res.*, **57**, 1039–1048.

Zhou, M., Zhu, Y., Dorland, R. D., and Measures, C. I., 2010b: Dynamics of the current system in the southern Drake Passage. *Deep-Sea Res. I*, **57**, 1039–1048.